Improved electric-thermal-aging multi-physics domain coupling modeling and identification decoupling of complex kinetic processes based on timescale quantification in lithium-ion batteries.

SHI, H., WANG, S., HUANG, Q., FERNANDEZ, C., LIANG, J., ZHANG, M., QI, C. and WANG, L.

2024

Improved electric-thermal-aging multi-physics domain coupling modeling and identification decoupling of complex kinetic processes based on timescale quantification in lithium-ion batteries

Haotian Shi[a], Shunli Wang[a*], Qi Huang[a], Carlos Fernandez[b], Jianhong Liang[c], Mengyun Zhang[a], Chuangshi Qi[a], Liping Wang[c*]

[a]*School of Information Engineering, Southwest University of Science and Technology, Mianyang 621010, China;*

[b]*School of Pharmacy and Life Sciences, Robert Gordon University, Aberdeen AB10-7GJ, UK;*

[c]*Department of Mechanical Engineering, Tsinghua University, Beijing 100084, China;*

Abstract: Unraveling the kinetic behavior inside the battery is essential to break through the limitations of mechanistic studies and to optimize the control of the integrated management system. Given this fact that the battery system is multi-domain coupled and highly nonlinear, an improved lumped parameter multi-physical domain coupling model is first developed to capture the electrical, thermal and aging characteristics of the battery in this paper. On this basis, an adaptive multi-timescale decoupled identification and estimation strategy is proposed based on the quantified timescale innovation, which realizes the online monitoring of the battery state and the accurate identification of the model parameters. The specific idea is that the decoupled identification of kinetic parameters inside the cell, the terminal voltage prediction and the real-time monitoring of the internal temperature with the online estimation of the available capacity are distinguished under different timescales. Meanwhile, the response time characteristic of the different kinetics is extracted and analyzed as a distinction between the coupled internal electrochemical processes. In this idea, four functionally different sub-observers are developed independently. Significantly, adaptive time-scale driven methods designed based on the fundamental timescale of the system, the amount of variation of the state of charge, and the amount of transfer charge are used separately for the observer implementation at different timescales. In addition, the coupling of the fast and slow kinetic parameter discriminators is achieved by diffusion voltage, and the internal

temperature observer as well as the available capacity observer are coupled to each other based on the estimation results. Experimental results for two long-time operating conditions at 5, 25 and 45 °C show that the proposed strategy has fast convergence and reliable accuracy in monitoring the battery state characteristics. Compared with the traditional fixed timescale algorithm, the proposed multi-physics domain coupling modeling strategy based on independent timescale driven design is more competitive in practical embedded applications.

Keywords: Lithium-ion battery; Complex kinetic processes; Multi-physics coupled domain model; Timescale identification decoupling; Multi-characteristic modeling; Multi-state detection

***Corresponding authors at**: School of Information Engineering, Southwest University of Science and Technology, Mianyang 621010, China (S. Wang). State Key Laboratory of Tribology and Institute of Manufacturing Engineering, Department of Mechanical Engineering, Tsinghua University, Beijing 100084, China (L. Wang).

***E-mail address**:* wangshunli@swust.edu.cn (S. Wang), lpwang@mail.tsinghua.edu.cn (L. Wang).

1 Introduction

1.1 Motivation and challenges

Rechargeable lithium-ion batteries, an important part of the clean energy network, are an alternative to petroleum-based fuels for achieving global decarbonization plans [1-4]. Secondary energy products, mainly lithium-ion batteries, have become an integral part of contemporary life. To improve the application safety and endurance of battery energy systems, the development of advanced and reliable battery management systems (BMS) is still a hot research topic nowadays [5,6]. Known as a black box, the lithium-ion battery system has a complex behavior of multiple physical domains including electrical, thermal, and mechanical inside [7]. The modeling approach based under a single physical domain seems to be slightly inadequate in accurately characterizing the complex dynamical behavior inside the cell.

The challenge of clarifying and extracting the behavior of complex kinetic characteristics information in multiple physical domains inside the battery, which plays a crucial role in modeling the battery throughout its life cycle.

Unraveling the kinetic characteristic behavior inside the battery can guide the development of an advanced BMS and performance optimization during cycling. As studied in the Refs. [8,9], the kinetic response exhibits specific timescale information that can be used to analyze the current performance state of the battery. Taking the disassembly approach is one of the ways to obtain the timescale information, which likewise has a devastating effect on the battery. Fortunately, the different response time characteristics exhibited by the kinetic behavior processes of carriers inside the cell provide a non-destructive way of capturing time-scale information [10]. In this form, high precision characterization of the complex kinetic behavior inside the battery can be achieved by differentiating and quantifying the timescale information [7]. Extracting and quantifying the timescale information of different kinetic responses gives a completely new path to the multi-physics domain coupling modeling of batteries and the development of advanced BMS.

1.2 Literature review

From the viewpoint of different physical domain functions and user usage, battery electrical characteristic modeling is the core of the whole BMS, thermodynamic characteristic modeling is the key, and aging characteristic modeling is the foundation. From the perspective of functional definition of internal state, the accurate estimation of state of charge (SOC), which characterizes the current remaining battery power, has a direct impact on the future behavior plan of the user [11,12]. Online temperature monitoring, especially the internal temperature, determines the overall system safety [13]. The current available capacity of the battery can optimize the performance of the entire BMS system and control the

energy output scheme [14]. Therefore, coupled multi-physics domain modeling and state estimation that balances computational complexity as well as consideration of complex kinetic behavior is an integral part of advanced BMS systems. Accurate monitoring of the SOC, internal temperature, and available capacity of the battery should be a priority throughout the life cycle of the installed battery application.

In the current existing work on battery modeling, many methods have been studied for problem solving in the electrical, thermodynamic and aging properties. The typical methods for modeling the electrical properties include electrochemical mechanism models [15,16], equivalent circuit models [9,17], and electrochemical impedance models [18,19]. The electrochemical mechanism model can characterize the macroscopic and microscopic features of the battery more comprehensively, and the more parameters to be identified make algorithms in the embedded application of the rapidity and stability cannot be effectively guaranteed [7,11]. Both electrochemical impedance curve-based and data-driven electrical characteristic modeling have extremely high computational complexity, which makes them still a huge technical challenge in current embedded applications [20,21]. In contrast, the equivalent circuit model is the most widely used in battery embedded systems due to its relative simplicity and reliable accuracy. However, the inability to capture the complex kinetic behavior inside the battery is a non-negligible drawback of the traditional equivalent circuit model.

In addition, distributed parameter thermal models based on partial differential equations and collective parameter thermal models based on thermodynamic energy balance equations are commonly used modeling methods in thermodynamic characterization [11,22-24]. The aging characteristic of batteries is commonly characterized by electrochemical mechanism models as well as data-based empirical models. More typical works include the battery health prediction studies conducted by Che et al. [25-28] based on neural networks and migration learning. Meanwhile, Hu et al. [29] also achieved

battery health status monitoring based on a fused feature selection and machine learning approach. Also, Severson et al. [30] and Tian et al. [31,32] trained a model with a partial pre-recession dataset and achieved the prediction of battery cycle life under full life cycle based on a deep learning network. In fact, the modeling of electrical and thermodynamic characteristics is also achievable through the data-driven class of methods based on neural networks and their variants, without considering the computer performance and the data storage cost conditions [33-37]. However, none of the modeling strategies mentioned above in the literature is a lightweight solution. Although current computer technology has been progressed, the computational complexity requirement is still a factor that cannot be ignored in current battery embedded system applications.

In order to more fully reveal the coupling relationship between different physical domains inside the battery, scholars have also been committed to developing electro-thermal coupling models to accurately simulate the dynamic characteristics of the battery. The more typical modeling methods include combining the partial differential equation-based electro-thermal coupling model and the centralized parameter-based electro-thermal coupling model. Electro-thermal coupling models dominated by partial differential equations are usually realized by a combination of electrical property models based on electrochemical mechanistic modes and thermal models based on heat generation equations [38,39]. In this regard, Xu et al. [40,41] realized the development of a thermoelectric coupling model by using a simplified two-dimensional electrochemical mechanism model in combination with a lumped parameter thermal model. Additionally, Wang et al. [42,43] constructed a fractional-order thermoelectric coupling model of the battery based on electrochemical impedance spectroscopy, which also realizes the characterization of the kinetic properties of the battery. It is worth affirming that all of the above methods have remarkable reliability and accuracy in the characterization of electro-thermal

coupling properties. However, the computational complexity associated with the large number of partial differential equation systems largely constrains the application of the above modeling methods in embedded systems.

Driven by the above issues, the lumped parameter-based electro-thermal coupling model shows great potential for development due to its relative simplicity and reliable accuracy. The lumped parameter electro-thermal coupling model usually consists of an equivalent circuit electrical sub-model and a lumped parameter thermal sub-model, which is of great value for scientific and engineering applications as it significantly reduces the computational complexity of modeling systems between multi-physical domains [44,45]. However, the traditional equivalent circuit model is only effective in supervising the realization of macro-voltage and current parameters, and is unable to capture the complex kinetic behavior inside the battery. The lack of explanation of the internal kinetics of the battery is also a non-negligible drawback of the lumped parameter electro-thermal coupling model.

Fortunately, the different kinetic responses and the decay of the battery performance all exhibit specific timescale information, which provides a promising opportunity to model the internal complex kinetic behavior from different timescales. The complex kinetic processes of the battery are characterized at the micro level by internal carrier movement, interfaces and various non-homogeneous interfacial response features, which are elaborated in detail in the study of Zhang et al. [7]. These micro kinetic processes can be described by ohmic polarization, concentration polarization, electrochemical polarization and thermal energy conduction processes in equivalent circuit modeling. In this case, the different kinetics processes can be decoupled into two parts: fast and slow kinetic [46]. In fact, the capacity decay characterizing battery aging during cycling exhibits longer timescale information than the changes in terminal voltage and temperature [47-49]. From the whole life cycle perspective, it is a

reasonable solution to model the aging characteristic at large timescale and the electro-thermal characteristics at small timescale, respectively, and to couple them in a multi-physical domain composite model through a feedback mechanism.

Based on the above discussions, a framework for multi-physics domain coupling modeling can be initially formulated based on timescale discrepancy information. At this point, the choice of algorithms for the estimation of different states and the way of quantifying the time-scale are supposed to be considered. Under the premise that many algorithms can achieve the above functions, light-weight algorithms based on recursive least squares (RLS) [50-52] and extended Kalman filter (EKF) [53-55] are still the most valuable options for embedded applications at present considering the computational complexity factor of multi-physics domain coupling modeling. Given the facts described above, the forgetful factor recursive least squares (FFRLS) algorithm and the EKF algorithm are selected to develop state monitors in multi-physics domain coupling modeling in this paper. On different time-scales driven by the observer, the sampling time of the system can be seen as the basic timescale property. Meanwhile, the driver of the slow kinetic algorithm in small timescale can be designed based on the amount of SOC variation. The execution of the battery capacity estimation algorithm in large timescale can be achieved by quantifying the amount of charge transferred.

1.3 Idea and contributions

With the goal of achieving non-destructive characterization of complex kinetic and accurate monitoring of different states, this paper constructs a multi-physics domain coupled model considering electrical, thermal and aging properties. Meanwhile, an efficient adaptive multi-timescale decoupled identification and estimation strategy is proposed based on the quantified timescale innovation. The four main contributions make this research different from existing ones.

(1) An improved multi-physics domain coupled model is constructed to model the electrical, thermal and aging properties of the battery with the smallest possible error.

(2) An efficient adaptive multi-timescale decoupled identification and estimation strategy is proposed to maximize the modeling of the complex kinetic behavior of the battery at different timescales.

(3) Quantitative time-scale features are analyzed and extracted, thus decoupling the complex kinetic behavior within the battery in a non-destructive form and improving the accuracy of the kinetic interpretation.

(4) The development of sub-observers on different timescales is coupled to each other, and the drivers of the three sub-algorithms with different functionalities are designed to be independent and highly adaptive.

1.4 Paper organization

The remainder of this paper is organized as follows: Section **2** introduces the coupled multi-physics domain model considering electrical, thermal and aging properties and the model-based state-space characterization method. Section **3** proposes an efficient adaptive multi-timescale decoupled identification and estimation strategy and completes the design of each sub-observer in the strategy based on the quantized timescale innovation. Section **4** presents experiments and results analysis on the identification of kinetic parameters, the effect of terminal voltage tracking, the estimation accuracy of internal temperature and the estimation effect of available capacity. And the conclusions are given in Section **5**.

2 Electric-thermal-aging multi-physics domain coupling modeling

2.1 Lumped parameter multi-physics domain coupled model

The multi-physics coupled domain model (MPDCM) based on timescale information of complex kinetic processes is used to characterize the electrical-thermal-aging of lithium-ion batteries in this paper. The MPDCM is represented as an electrothermal characteristic at small timescale as well as an aging characteristic at large timescale, as shown in Fig. 1. Meanwhile, based on the timescale differences in the electrochemical reactions inside the cell during charging and discharging, the electrical behavior at small timescale is characterized as fast kinetic as well as slow kinetic processes.

Based on the modeling idea of timescale quantization, a second-order resistance-capacitance (RC) equivalent circuit network with significantly different time constants, as shown in sub-Fig. 1(a), is used to describe the electrical behavior of the battery. Meanwhile, the accuracy as well as the relative simplicity of the model has been demonstrated in many works. Moreover, considering the computational complexity required for multi-physics domain modeling of the lumped parameter, a simplified thermal path model, as in sub-Fig. 1(b), is used in this paper for real-time online estimation of the battery internal temperature. Meanwhile, the results of entropy heat coefficient acquisition under the experiment are combined to achieve effective modeling of the battery heating power. In addition, the slowly capacity decay phenomenon is one of the most obvious characteristics of battery aging. The estimation of the available battery capacity using different time-scale control strategies at large timescale is also considered in this paper, as shown in sub-Fig. 1(c).

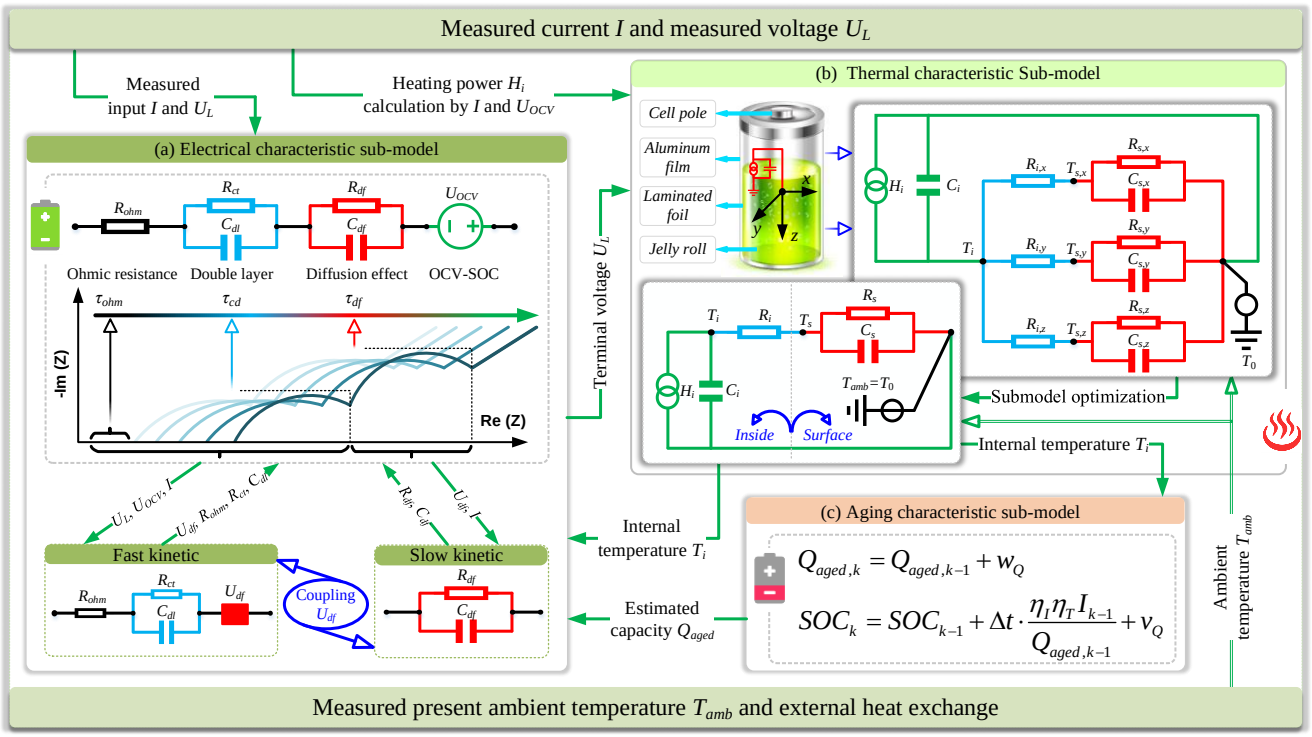

Fig. 1. Structure view of lumped parameter electric-thermal-aging multi-physics domain coupled model: (a) Electrical characteristic sub-model; (b) Thermal characteristic sub-model; (c) Aging characteristic sub-model.

In sub-Fig. 1(a), R_{ohm} denotes the ohmic internal resistance, U_{OCV} is the open-circuit voltage (OCV) of the cell, R_{ct} in the dual RC link is the charge transfer resistance, C_{dl} denotes the bilayer capacitance, R_{df} denotes the diffusion resistance, C_{df} is the diffusion capacitance, and U_{df} is the diffusion voltage of R_{df} and C_{df} the link. The parallel connection of $R_{ct}C_{dl}$ and $R_{df}C_{df}$ are used to simulate the electrochemical polarization and the concentration polarization processes of the cell, respectively. In addition, τ_{ohm}, τ_{cd} and τ_{df} denote the reaction time of ohmic effect, double layer effect and diffusion effect, respectively. Based on the Nyquist curve of the cell it can be observed that the three behave numerically as $\tau_{ohm} < \tau_{cd} \ll \tau_{df}$. Naturally, this provides a clear direction for the capture of the kinetic properties at different timescales.

In sub-Fig. 1(b), the three-dimensional cell thermal pathology is first modeled with subscripts x, y, and z in each component indicating three mutually perpendicular directions. Where, H_i is the heat producing power of the battery, T_i indicates the highest internal temperature point of the battery, C_i

characterizes the internal equivalent heat capacity, R_i characterizes the internal equivalent heat resistance, T_s characterizes the surface temperature of the battery, R_s characterizes the external equivalent heat resistance, and C_s characterizes the equivalent heat capacity of the battery case. It is worth indicating that aluminum-cased cylindrical NCM battery is chosen to be used for experimental analysis in this paper. The internal and external thermodynamic parameters of this battery type remain essentially the same in different directions. Considering the computational complexity and modeling accuracy, the optimized single-dimensional thermal pathology model is adopted in this paper. In sub-Fig. 1(c), Q is the actual capacity of the cell. w_Q is characterized as state noise. which is used to model the slow change process of the battery available capacity. w_Q is characterized as the observation noise. The MPDCM can be designed by quantized time-scale driven design to achieve the cooperative estimation of terminal voltage, internal temperature and capacity of the battery at different timescales.

2.2 MPDCM-based modular state-space equation representation

2.2.1 Electrical characteristic sub-model at small timescale

For the electrical characteristic sub-model at small time scales, the electrochemical reactions inside the cell are separated and modeled as fast as well as slow kinetic processes based on response time differences. Based on this idea, we define the current of the battery to be positive when charging and negative when discharging. At this point, the electrical characteristic sub-model can be described by the linear discrete equation shown in Equation (1).

$$U_{cd,k} = e^{-\frac{\Delta t}{\tau_{cd}}} U_{cd,k-1} + (1 - e^{-\frac{\Delta t}{\tau_{cd}}}) R_{ct,k} I_{k-1} \tag{1a}$$

$$U_{df,k} = e^{-\frac{\Delta t}{\tau_{df}}} U_{df,k-1} + (1 - e^{-\frac{\Delta t}{\tau_{df}}}) R_{df,k} I_{k-1} \tag{1b}$$

In Equation (1), Δt is the time interval between two consecutive sampling points. I_{k-1} denotes

the current at the k-1th sampling point. $U_{cd,k}$ and $U_{cf,k}$ denote U_{cd} and U_{cf} at the kth sampling point, respectively. As mentioned above, τ_{cd} is numerically much smaller than τ_{df}, and they are calculated as $\tau_{cd} = R_{ct}C_{dl}$ and $\tau_{df} = R_{df}C_{df}$, respectively. Among them, τ_{cd} is used to capture the charge transfer and the double layer effect under fast kinetic, and τ_{df} is used to capture the diffusion effect of active lithium at the solid-phase particle interface under slow kinetic. Further, the terminal voltage of the electrical characteristic sub-model based on the second-order RC network in combination with the ohmic effect can be calculated by Equation (2).

$$U_{L,k} = f_{OCV}(SOC_k, T_{i,k}) + I_k R_{ohm,k} + U_{cd,k} + U_{df,k} \tag{2}$$

In Equation (2), $U_{L,k}$, SOC_k and $T_{i,k}$ denote the battery terminal voltage value, SOC value and internal temperature value at the kth sampling point, respectively. f_{OCV} denotes the expression of OCV as a function of SOC as well as T_i at the kth sampling point. Without loss of generality, the subscripts k as well as k-1 denote the kth and k-1th sampling point in the next part of this paper, respectively.

It is worth mentioning that many methods are available to achieve high accuracy estimation of the battery SOC. The precision of SOC calculation based on the ampere-hour counting (AHC) is equally acceptable, when the initial value can be obtained precisely in the laboratory. In addition, the accurate estimation of the actual battery capacity at large timescale is implemented in this paper using an independently developed estimator. At this point, the real-time SOC of the battery combining the actual capacity as well as the AHC method is calculated as shown in Equation (3).

$$SOC_k = SOC_{k-1} + \Delta t \cdot \frac{\eta_I \eta_T I_{k-1}}{Q_{aged,k-1}} \tag{3}$$

In Equation (3), Q_{aged} is the actual capacity of the battery after aging. η_I is the Coulomb efficiency factor. η_T is the temperature efficiency factor. Both of them can be obtained by experimental calibration. In the laboratory case, the relationship between SOC, T_i and OCV can be solved easily by

means of building three-dimensional data tables. The real-time estimation of the battery capacity and the internal temperature is achieved using the developed estimator. Further, the accurate calculation of OCV can be achieved by a three-dimensional interpolation function.

2.2.2 Thermal characteristic sub-model at small timescale

The safe and stable operation of the battery embedded system cannot be separated from the real-time monitoring of the temperature, especially the internal temperature of the battery. In addition, the parameter updates in the Lumped parameter MPDCM are closely related to temperature. Therefore, it is significant to develop a temperature estimator and achieve real-time accurate estimation of the internal temperature of the battery at small time scales. Considering the effect of computational complexity, the principle of the modeling similarity of same-order systems is cleverly applied in this paper. As suggested in the Refs. [7,56], the accurate calculation of battery heat production can be achieved based on the Bernardi formula derived from the first law of thermodynamics. Because the classical Bernardi formula with many inputs has a large impact on the application of embedded systems, this paper focuses on the effect of current and internal resistance on the heat generation power. Based on this modeling idea, the heat source equation of the cell considering the polarization heat, the Joule heat and the reaction heat is proposed as shown in Equation (4).

$$H_{i,k} = f_{OCV}(SOC_k, T_{i,k})I_k - U_{L,k}I_k + I_k T_{i,k}\, dU_{OCV}/dT \tag{4}$$

In Equation (4), $H_{i,k}$ is the heat production power of the cell and represents the heat generation of the cell at moment k. $f_{OCV}(SOC_k, T_{i,k})I_k - U_{L,k}I_k$ is used to characterize the polarization heat and Joule heat of the cell. The differential term dU_{OCV}/dT represents the entropy heat coefficient and T is the Calvin temperature of the cell. It is worth mentioning that the entropy heat coefficient of the cell is used to calculate the chemical reaction heat production of the cell. Its value is available in advance under

laboratory conditions. Further, based on the similarity principle for modeling systems of the same order, the optimized battery thermal circuit model shown in sub-Fig. 1(b) can be described by the state-space equation in the time-domain state as shown in Equation (5).

$$\frac{dT_{ia}}{dt} = -\frac{T_{ia}}{R_i C_i} + \frac{T_{sa}}{R_i C_i} + \frac{H_i}{C_i} \tag{5a}$$

$$\frac{dT_{sa}}{dt} = -\frac{T_{ia}}{R_i C_s} + \frac{T_{sa}}{R_i C_s} + \frac{T_{sa}}{R_s C_s} \tag{5b}$$

In Equation (5), T_{ia} is the relative difference between the internal temperature of the cell and the ambient temperature, which is calculated as $T_{ia} = T_i - T_{amb}$. Similarly, T_{sa} is the relative difference between the surface temperature and the ambient temperature, which is calculated as $T_{sa} = T_s - T_{amb}$. It is worth noting that the spatial equation expression in the time domain state is not suitable for embedded applications in battery systems. At this point, the nodes T_i and T_s in the thermal characteristic sub-model are discrete using the first-order forward difference method, and the linear discrete form of Equation (5) is obtained as shown in Equation (6).

$$\begin{bmatrix} T_{ia,k+1} \\ T_{sa,k+1} \end{bmatrix} = \begin{bmatrix} 1-\frac{\Delta t}{R_i C_i} & \frac{\Delta t}{R_i C_i} \\ \frac{\Delta t}{R_i C_s} & 1-\left(\frac{\Delta t}{R_i C_s} + \frac{\Delta t}{R_s C_s}\right) \end{bmatrix} \begin{bmatrix} T_{ia,k} \\ T_{sa,k} \end{bmatrix} + \begin{bmatrix} \frac{\Delta t}{C_i} \\ 0 \end{bmatrix} \begin{bmatrix} H_{i,k} \end{bmatrix} \tag{6a}$$

$$T_{sa,k+1} = \begin{bmatrix} 0 & 1 \end{bmatrix} \begin{bmatrix} T_{ia,k} \\ T_{sa,k} \end{bmatrix} + \begin{bmatrix} 0 \end{bmatrix} \begin{bmatrix} H_{i,k} \end{bmatrix} \tag{6b}$$

In Equation (6), $T_{ia,k}$ and $T_{sa,k}$ denote the T_{ia} and T_{sa} values of the battery at moment k, respectively, and $T_{ia,k+1}$ and $T_{sa,k+1}$ have the same meaning. Δt denotes the time interval of two consecutive sampling points of the system.

2.2.3 Aging characteristic sub-model at large timescale

Given the fact that battery capacity decay is one of the most direct features of battery aging, accurate

and reliable estimates of the current battery capacity available are essential for the management and optimization of the entire battery system. For modeling the battery aging characteristic, the available capacity remains essentially constant over a shorter number of charges and discharges compared to the more pronounced changes in terminal voltage, SOC and internal temperature over small timescale. Distinguishing the timescale difference between battery available capacity estimation and other state prediction can improve the computational efficiency of coupled multi-physics domain modeling while ensuring accuracy. For the above reasons considered, the state-space equation of the battery aging state sub-model is obtained as shown in Equation (7) by combining the capacity slow change pattern and the AHC method.

$$Q_{aged,k} = Q_{aged,k-1} + w_Q \tag{7a}$$

$$SOC_k = SOC_{k-1} + \Delta t \cdot \eta_I \eta_T I_{k-1} / Q_{aged,k-1} + v_Q \tag{7b}$$

Equations (7a) and (7b) are the state equation and observation equation of the capacity estimation sub-model in the discrete state, respectively. The slowly varying process of Q_{aged} at large time scales is elucidated in Equation (7a), and this process is modeled by Gaussian white noise w_Q with zero mean. The AHC-based SOC values are considered to be of high accuracy due to the initial values of the battery SOC in the laboratory case can be known. It can be chosen as an observation for the capacity estimation state-space equation whose observation noise is modeled by a Gaussian white noise v_Q with zero mean.

3 MPDCM-based kinetic parameter identification and state estimation

3.1 Timescale separation and decoupling identification architecture

As mentioned above, the battery capacity in the MPDCM with the kinetic parameters, the terminal voltage and the internal temperature are estimated on different timescales. In addition, the identification

of the model parameters is also decoupled into fast and slow kinetic components. Based on the above idea, an adaptive multi-timescale decoupled identification and estimation (AMTDIE) strategy is proposed in this paper to achieve lossless characterization of kinetic parameters and online monitoring of battery status. The difference with the fixed time scale modeling approach is that the proposed AMTDIE strategy extracts and quantifies the different timescale innovations used to decouple the complex kinetic behavior inside the battery. A distinct advantage is that the strategy can achieve high-fidelity modeling of the internal battery kinetic processes in a nondestructive form, further enabling efficient synergistic prediction of model parameters and battery states. The modeling principle based on separation of timescales and decoupling of complex kinetic identification is shown in Fig. 2.

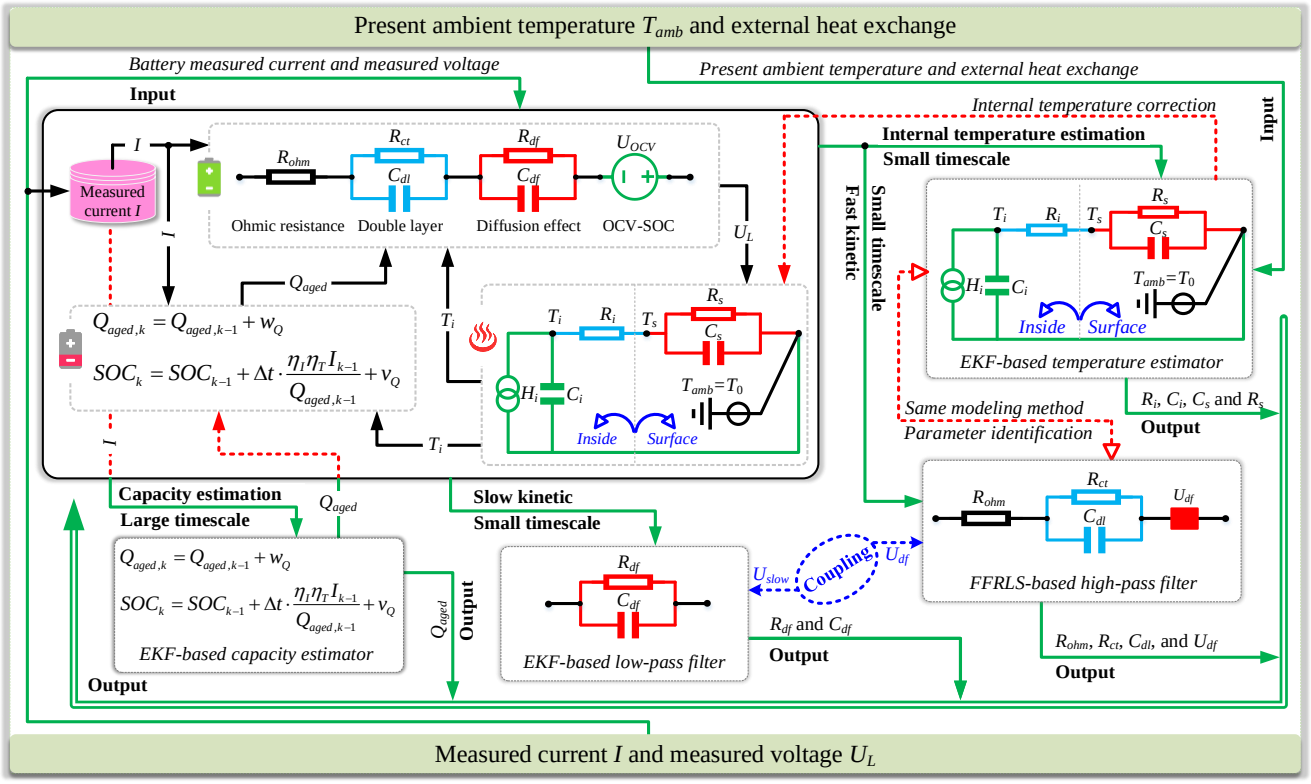

Fig. 2. Modeling principles for timescale separation and decoupling identification of complex kinetic.

As shown in Fig. 2, the idea of timescale separation and complex kinetic decoupling identification naturally distinguishes the kinetic parameter identification, SOC calculation, and internal temperature estimation at small timescale from the battery available capacity estimation at large timescale. In addition,

the electrochemical polarization parameters and thermal pathology parameters in the fast kinetic and the concentration difference polarization parameters in the slow kinetic are similarly separately identified at small timescale. In the small timescale of the whole modeling strategy, the identification of ohmic polarization parameters, electrochemical polarization parameters and full parameters of thermal pathology under fast kinetic is realized by a high-pass filter based on the FFRLS algorithm. The estimation of battery internal temperature is realized by a high-pass state estimator based on the EKF algorithm. The identification of slow kinetic parameters is realized by a low-pass filter based on the EKF algorithm. Meanwhile, the estimation of the battery available capacity is implemented in a larger timescale by the EKF-based algorithm.

Three points are worth stating here throughout the decoupled modeling process. First, the fast kinetic parameters in the electrical characteristic sub-model are coupled with those of the slow kinetic parameters via diffusion voltage, both of which work together for accurate estimation of the battery terminal voltage. Second, the internal temperature estimation results of the thermal characteristic sub-model optimize the calculation of the OCV and entropy thermal coefficient in real-time, which further improves the estimation accuracy of the battery terminal voltage and the available capacity. Third, the battery capacity prediction results are also fed back to the electrical characteristic sub-model in real-time, which is used to optimize the accuracy of the AHC-based SOC iteration.

3.2 Identification decoupling of complex dynamic in small timescale

3.2.1 Design of FFRLS-based fast kinetic parameter discriminator

The parameters to be identified under fast kinetic in small timescale include R_{ohm}, R_{ct}, C_{dl}, R_i, C_i, R_s and C_s. First, we define the sum of the voltages of the R_{ohm}, $R_{ct}C_{dl}$ and $R_{df}C_{df}$ links as U_p.

In this case, the U_p can be obtained from the difference between the battery terminal voltage U_L and the open-circuit voltage. Then, the difference equations of the electrical and thermal sub-models under fast kinetic are derivable according to Equations (1) and (6), as shown in Equation (8).

$$U_{p,k} = \alpha_1 U_{p,k-1} + \alpha_2 I_k + \alpha_3 I_{k-1} + \alpha_4 \tag{8a}$$

$$T_{ia,k} = \beta_1 T_{ia,k-1} + \beta_2 T_{ia,k-2} + \beta_3 H_{i,k-1} + \beta_4 H_{i,k-2} \tag{8b}$$

In Equation (8), $\alpha_1, \alpha_2, \alpha_3, \alpha_4, \beta_1, \beta_2, \beta_3$ and β_4 are the coefficients to be identified for the difference equation under fast kinetic, and their specific expansion form is shown in Equation (9).

$$\alpha_1 = R_{ct}C_{dl}/(\Delta t + R_{ct}C_{dl}), \alpha_2 = ((R_{ohm} + R_{ct})\Delta t + R_{ohm}R_{ct}C_{dl})/(\Delta t + R_{ct}C_{dl}) \tag{9a}$$

$$\alpha_3 = -R_{ohm}R_{ct}C_{dl}/(\Delta t + R_{ct}C_{dl}), \alpha_4 = ((\Delta t + R_{ct}C_{dl})U_{df,k} - R_{ct}C_{dl}U_{df,k-1})/(\Delta t + R_{ct}C_{dl}) \tag{9d}$$

$$\beta_1 = -\Delta t/R_iC_i - \Delta t/R_sC_s - \Delta t/R_iC_s + 2, \beta_2 = (1 - \Delta t/R_iC_i)(\Delta t/R_sC_s + \Delta t/R_iC_s - 1) \tag{9e}$$

$$\beta_3 = \Delta t/C_i, \beta_4 = (\Delta t/C_i)(\Delta t/R_sC_s + \Delta t/R_iC_s - 1) \tag{9g}$$

Further, we write the difference equation shown in Equation (8) in the form of an exogenous autoregressive equation, as shown in Equation (10).

$$\underbrace{\begin{bmatrix} U_{p,k} \\ T_{ia,k} \end{bmatrix}}_{\boldsymbol{y}_{fast,k}} = \underbrace{\begin{bmatrix} \alpha_{1,k} & \alpha_{2,k} & \alpha_{3,k} & \alpha_{4,k} \\ \beta_{1,k} & \beta_{1,k} & \beta_{1,k} & \beta_{1,k} \end{bmatrix}}_{\boldsymbol{\theta}_{fast,k}} \underbrace{\begin{bmatrix} U_{P,k-1} & I_k & I_{k-1} & 1 \\ T_{ia,k-1} & T_{ia,k-2} & H_{i,k-1} & H_{i,k-2} \end{bmatrix}^T}_{\boldsymbol{h}_{fast,k}} \tag{10}$$

In Equation (10), $\boldsymbol{\theta}_{fast,k}$ is the generation identification coefficient matrix, $\boldsymbol{h}_{fast,k}$ is the data input matrix, $\boldsymbol{y}_{fast,k}$ is the data output matrix. To avoid the problem of iterative failure due to data saturation, the FFRLS algorithm is chosen for parameter identification under fast kinetic in small timescale. At this point, the core iterative process of the FFRLS algorithm is shown in Equation (11) in combination with Equation (10).

$$\hat{\boldsymbol{\theta}}_{fast,k} = \hat{\boldsymbol{\theta}}_{fast,k-1} + L_{fast,k}(\boldsymbol{y}_{fast,k} - \hat{\boldsymbol{\theta}}_{fast,k-1}\boldsymbol{h}_{fast,k}^T) \tag{11a}$$

$$L_{fast,k} = (\boldsymbol{P}_{fast,k-1}\boldsymbol{h}_{fast,k})/(\lambda + \boldsymbol{h}_{fast,k}^T\boldsymbol{P}_{fast,k-1}\boldsymbol{h}_{fast,k}) \tag{11b}$$

$$\boldsymbol{P}_{fast,k} = (\boldsymbol{P}_{fast,k-1} - L_{fast,k}\boldsymbol{h}_{fast,k}^{T}\boldsymbol{P}_{fast,k-1})/\lambda \tag{11c}$$

In Equation (11), $L_{fast,k}$ is the FFRLS gain at moment k, λ is the forgetting factor. $\widehat{\boldsymbol{\theta}}_{fast,k}$ is the estimate of the parameter matrix $\boldsymbol{\theta}_{fast,k}$ to be identified, $P_{fast,k}$ is the covariance matrix, and they are initialized as $\widehat{\boldsymbol{\theta}}_{fast,0} = \mathrm{E}[\boldsymbol{\theta}_{fast,0}]$ and $P_{fast,0} = \mathrm{E}[(\boldsymbol{\theta}_{fast,0} - \widehat{\boldsymbol{\theta}}_{fast,0})(\boldsymbol{\theta}_{fast,0} - \widehat{\boldsymbol{\theta}}_{fast,0})^{T}]$. With the help of the FFRLS algorithm and the experimental data set, the coefficients to be identified for the difference equation under fast kinetic are obtained under each moment. Further, the values of the fast kinetic parameters and the diffusion voltage U_{df} are iteratively identified by Equation (9). Also, the terminal voltage U_L in the MPDCM is also can be calculated in real-time by Equation (2). In addition, based on the debugging results of the data set at different temperatures, we set the value of λ to 0.99 in this paper.

3.2.2 Design of EKF-based slow kinetic parameter discriminator

The parameter identification of complex kinetic processes inside the cell, such as ohmic polarization, electrochemical polarization, concentration difference polarization, and thermodynamic conduction, are set in small timescale in this paper. As mentioned in our previous study [46], the response times of complex kinetic processes inside the cell are not distributed in the same frequency range. Therefore, the parameter under slow kinetic at small timescale is proposed to be separately identified at separate time scales. A natural solution is to implement the control of the slow kinetic algorithm drive in the fixed-step form, and the rationality of this solution is also verified by previous studies [8]. However, an obvious disadvantage is that the design of the fixed-step scheme is rather harsh in the selection of operating conditions. When the battery pack embedded system is under frequent charging and discharging conditions, the time constants of the concentration difference process based on the fixed-step drive control will be significantly smaller. This makes the discrimination results of slow kinetic

parameters exhibit large dispersion and entropy values [17]. In addition, too large fixed-step design can lead to distortion of the algorithm when identifying fast kinetic parameters, while too small a fixed-step design can easily lead to data saturation in the identification of slow kinetic parameters.

To effectively avoid the above problems, an adaptive drive timescale design is employed for performing the identification of slow kinetic parameters in this paper. It is not difficult to observe from the electrical characteristic sub-model that the loading current of the concentration difference polarization link also acts on the OCV-SOC link. Therefore, the drive design used for the slow kinetic sub-algorithm can be implemented by the amount of SOC variation as shown in Equation (12).

$$\Delta SOC = \Delta t \cdot \sum_{k=1}^{m} \eta_I \eta_T I_k / Q_{aged,k} \tag{12}$$

In Equation (12), ΔSOC represents the battery SOC variation during time $k = 1{:}\,\mathrm{m}$, and m is the number of steps to run this slow kinetic parameter identification algorithm, and its value will change adaptively according to the current excitation conditions. In this paper, we set the driving threshold of the slow kinetic sub-algorithm to $\Delta SOC \geq 0.5\%$ by combining the degree of nonlinearity of the OCV-SOC relationship curve. That is, the sub-filter used to identify the slow kinetic parameter identification will be executed automatically when the amount of battery SOC variation under current excitation exceeds 0.5%. It can also be seen from Equation (12) that the current integration in discrete form takes into account the system charging and discharging directions. One of the most obvious advantages is that the designed scheme can be adaptive to arbitrary operating conditions, thus solving the problem of improving the generality of multi-physics domain coupling modeling.

One point of clarification is that from Equation (12), it can be found that the time scale of the slow kinetic sub-algorithm changes adaptively with the C-rate. However, under the SOC-based adaptive driver design, the effect of the C-rate is actually included in the calculation of ΔSOC. The whole battery

system at this point does not care how many iterations have actually been performed. As long as the amount of change in SOC reaches the constraints of the system, then the change in terminal voltage also contains enough valid information, which in turn makes the slow kinetic sub-algorithm execute stably and go on effectively. The fast kinetic sub-algorithm driver, on the other hand, uses the sampling time of the actual embedded system. With current computer technology, the sampling time of the embedded system can often reach a very high frequency. In this way, the fast kinetic sub-algorithm and slow kinetic sub-algorithm are reasonably and efficiently distinguished at small timescale.

Further, to achieve high accuracy identification of slow kinetic parameters, a low-pass sub-filter based on the EKF algorithm is developed in this paper. First, we define the state variable of the low-pass sub-filter at small timescale as $\boldsymbol{\theta}_{slow} = [R_{df}\ C_{df}]$. At this point, the state-space equation of the concentration difference polarization link can be described in the form shown in Equation (13).

$$\boldsymbol{\theta}_{slow,k+1} = \boldsymbol{\theta}_{slow,k} + \boldsymbol{w}_{slow} \tag{13a}$$

$$U_{slow,k+1} = e^{\frac{-\Delta t}{R_{df,k}C_{df,k}}} U_{slow,k} + (1 - e^{\frac{-\Delta t}{R_{df,k}C_{df,k}}}) R_{df,k} I_k + v_{slow} \tag{13b}$$

Equations (13a) and (13b) are the state and observation equations of the slow kinetic process in discrete form, respectively. The slowly varying process of the concentration difference polarization parameter is elucidated in Equation (13a), and this process is modeled by the noise w_{slow}. The port voltage of the concentration difference polarization link is chosen as the observed variable of the low-pass sub-filter at small timescale, denoted by the symbol U_{slow}, and its observation error is characterized by v_{slow}. In addition, both w_{slow} and v_{slow} are considered as Gaussian white noise with zero mean and covariance $Q_{slow,k}$ and $R_{slow,k}$, respectively. Further, we define the full-response equation of the concentration difference polarization link in the following form:

$$g\left(U_{slow,k}, I_k, \boldsymbol{\theta}_{slow,k}\right) = e^{\frac{-\Delta t}{R_{df,k}C_{df,k}}} U_{slow,k} + (1 - e^{\frac{-\Delta t}{R_{df,k}C_{df,k}}}) R_{df,k} I_k \tag{14}$$

Assuming that Equation (14) is derivable at all sample points, the first-order Taylor expansion can be used to calculate the system observation matrix C_{slow} for the low-pass parameter discriminator, which is shown in Equation (15).

$$\begin{aligned} C_{slow,k} &= \left.\frac{\partial g(U_{slow,k},I_k,\boldsymbol{\theta}_{slow,k})}{\partial \boldsymbol{\theta}_{slow}}\right|_{\boldsymbol{\theta}_{slow}=\hat{\boldsymbol{\theta}}^-_{slow,k}} \\ &= \left(\frac{\partial g\left(U_{slow,k},I_k,\boldsymbol{\theta}_{slow,k,}\right)}{\partial \boldsymbol{\theta}_{slow}} + \frac{\partial g\left(U_{slow,k},I_k,\boldsymbol{\theta}_{slow,k}\right)}{\partial U_{slow,k}}\cdot\frac{dU_{slow,k}}{d\boldsymbol{\theta}_{slow}}\right)\Bigg|_{\boldsymbol{\theta}_{slow}=\hat{\boldsymbol{\theta}}^-_{slow,k}} \\ &= \left(\left[\frac{\partial g\left(U_{slow,k},I_k,\boldsymbol{\theta}_{slow,k,}\right)}{\partial R_{df}} \quad \frac{\partial g\left(U_{slow,k},I_k,\boldsymbol{\theta}_{slow,k,}\right)}{\partial C_{df}}\right] + \frac{\partial g\left(U_{slow,k},I_k,\boldsymbol{\theta}_{slow,k}\right)}{\partial U_{slow,k}}\cdot\frac{dU_{slow,k}}{d\boldsymbol{\theta}_{slow}}\right)\Bigg|_{\boldsymbol{\theta}_{slow}=\hat{\boldsymbol{\theta}}^-_{slow,k}} \\ &= \left(\left[\frac{U_{slow,k}\Delta t - R_{df,k}I_k\Delta t}{(R_{df,k})^2 C_{df,k}} e^{\frac{-\Delta t}{R_{df,k}C_{df,k}}} + (1-e^{\frac{-\Delta t}{R_{df,k}C_{df,k}}})I_k \quad \frac{U_{slow,k}\Delta t - R_{df,k}I_k\Delta t}{R_{df,k}\left(C_{df,k}\right)^2} e^{\frac{-\Delta t}{R_{df,k}C_{df,k}}}\right] + e^{\frac{-\Delta t}{R_{df,k}C_{df,k}}}\cdot\frac{dU_{slow,k}}{d\boldsymbol{\theta}_{slow}}\right)\Bigg|_{\boldsymbol{\theta}_{slow}=\hat{\boldsymbol{\theta}}^-_{slow,k}} \end{aligned} \tag{15}$$

For the derivative term $dU_{slow,k}/d\boldsymbol{\theta}_{slow}$ in Equation (15), the further expansion is shown in Equation (16).

$$\frac{dU_{slow,k}}{d\boldsymbol{\theta}_{slow}} = \frac{\partial g\left(U_{slow,k-1},I_{k-1},\boldsymbol{\theta}_{slow,k-1}\right)}{\partial \boldsymbol{\theta}_{slow}} + \frac{\partial g\left(U_{slow,k-1},I_{k-1},\boldsymbol{\theta}_{slow,k-1}\right)}{\partial U_{slow,k-1}}\cdot\frac{dU_{slow,k-1}}{d\boldsymbol{\theta}_{slow}} \tag{16}$$

Combining Equations (15) and (16), it is easy to find that with the initialization of $dU_{slow,k}/d\boldsymbol{\theta}_{slow}$, $R_{df,k}$, $C_{df,k}$ and $U_{slow,k}$, the system can easily compute the observation matrix C_{slow} by iterative means. Then, with the state-space equation shown in Equation (13) available and the observation matrix C_{slow} known, the EKF algorithm is chosen to develop a low-pass parameter discriminator at small timescale due to its relative simplicity and reliable accuracy. The core iterative process of the EKF algorithm is shown in Equation (17).

$$\hat{\boldsymbol{\theta}}^-_{slow,k} = \hat{\boldsymbol{\theta}}^+_{slow,k-1} \tag{17a}$$

$$\boldsymbol{P}^-_{slow,k} = \boldsymbol{P}^+_{slow,k-1} + Q_{slow,k} \tag{17b}$$

$$K_{slow,k} = \boldsymbol{P}^-_{slow,k}\boldsymbol{C}^T_{slow,k}(\boldsymbol{C}_{slow,k}\boldsymbol{P}^-_{slow,k}\boldsymbol{C}^T_{slow,k} + R_{slow,k})^{-1} \tag{17c}$$

$$\hat{\boldsymbol{\theta}}^+_{slow,k} = \hat{\boldsymbol{\theta}}^-_{slow,k} + K_{slow,k}(U_{df,k} - h(U_{slow,k}, I_k, \hat{\boldsymbol{\theta}}^-_{slow,k})) \tag{17d}$$

$$\boldsymbol{P}^+_{slow,k} = \left(\boldsymbol{I} - K_{slow,k}\boldsymbol{C}_{slow,k}\right)\boldsymbol{P}^-_{slow,k} \tag{17e}$$

In the above iterations, Equations (17a) and (17b) represent the temporal update of the low-pass

parameter discriminator at small time scales, and Equations (17c), (17d) and (17e) represent the measurement update. In Equation (17), K_{slow} is the Kalman gain; $\widehat{\boldsymbol{\theta}}_{slow}^{-}$ and $\widehat{\boldsymbol{\theta}}_{slow}^{+}$ are the prior and posterior estimates of the state matrix, respectively, which is initialized by $\widehat{\boldsymbol{\theta}}_{slow,0}^{+} = \mathrm{E}[\theta_{slow,0}]$; P_{slow}^{-} and P_{slow}^{+} are the prior and posterior estimates of the error covariance, respectively, which is initialized by $P_{slow,0}^{+} = \mathrm{E}[(\boldsymbol{\theta}_{slow,0} - \widehat{\boldsymbol{\theta}}_{slow,0}^{+})(\boldsymbol{\theta}_{slow,0} - \widehat{\boldsymbol{\theta}}_{slow,0}^{+})^{T}]$. In addition, $dU_{slow,0}/d\boldsymbol{\theta}_{slow}$ and $U_{slow,0}$ are initialized with zero matrix, $R_{df,0}$ is initialized with 0 Ω, and $C_{df,0}$ is initialized with 150 kF in this paper.

A point worth stating is that the parameter identification under fast kinetic in small timescale can be iterated very quickly. Therefore, the converged U_{df} identification result based on the FFRLS algorithm is chosen as the true value of the end voltage of the electrochemical polarization link, and its reasonableness is proved in our previous study [17,45]. Further, when the driving threshold condition $\Delta SOC \geq 0.5\%$ of the slow kinetic sub-algorithm is satisfied, the EKF sub-algorithm will implement the iterative correction of $R_{df,k}$ and $C_{df,k}$ by the error between U_{df} and U_{slow}. At the same time, instructions to execute the low-pass parameter discriminator will be sent, which in turn will achieve accurate identification of the slow kinetic parameters on a specific timescale.

3.2.3 EKF-based design of high-pass internal temperature estimator

The accurate estimation of the battery temperature, especially the internal temperature, plays an important role in the safety monitoring of the whole embedded system. Considering the computational complexity impact of embedded applications, an optimized thermal pathology equivalent sub-model is constructed in this paper based on same-order system modeling similarity. Based on the state-space equation in discrete form under the thermal characteristic sub-model above, the EKF-based internal temperature state estimator is developed due to its relative simplicity and reliable accuracy. First, we

rewrite Equation (6) in a form that is convenient for EKF iterations, as shown in Equation (18).

$$x_{T,k+1} = \boldsymbol{A}_T x_{T,k} + \boldsymbol{B}_T u_{T,k} + w_T \tag{18}$$

$$y_{T,k} = \boldsymbol{C}_T x_{T,k} + \boldsymbol{D}_T u_{T,k} + v_T \tag{18}$$

In Equation (18), $H_{i,k}$ is chosen as the system input variable $u_{T,k}$ at moment k, $[T_{ia,k}\ T_{sa,k}]^T$ is the system state matrix $x_{T,k}$, and $T_{sa,k}$ is the observed variable $y_{T,k}$. In addition, w_T and v_T are the system process noise and observation noise of the thermal characteristic sub-model in the multi-physics domain coupling modeling, respectively, which are considered as Gaussian white noise with zero mean and covariance of Q_T and R_T, respectively. A_T, B_T, C_T, and D_T are matrix abbreviations for the state-space equations of the thermal circuit system, which are expanded in the form shown in Equation (19).

$$A_T = \begin{bmatrix} 1-\dfrac{\Delta t}{R_i C_i} & \dfrac{\Delta t}{R_i C_i} \\ \dfrac{\Delta t}{R_i C_s} & 1-\left(\dfrac{\Delta t}{R_i C_s}+\dfrac{\Delta t}{R_s C_s}\right) \end{bmatrix}, B_T = \begin{bmatrix} \dfrac{\Delta t}{C_i} \\ 0 \end{bmatrix}, C_T = [0 \quad 1], D_T = [0] \tag{19}$$

One obvious advantage of choosing T_{sa} as the observed variable for the thermal characteristic sub-model is that the cell surface temperature as well as the ambient temperature is much easier to measure than the internal temperature in the practical application of the battery. In addition, the accuracy of the heat source $H_{i,k}$ is equally crucial as the only input to the system. It is worth stating that the calculation of OCV is optimized by real-time feedback corrections of the battery available capacity and internal temperature in this paper. At this point, the core iterative process of the EKF sub-algorithm for the battery internal temperature estimation at small time scale is shown in Equation (20).

$$\hat{\boldsymbol{x}}_{T,k}^{-} = \boldsymbol{A}_{T,k-1}\hat{\boldsymbol{x}}_{T,k-1}^{+} + \boldsymbol{B}_{T,k-1}u_{T,k} \tag{20a}$$

$$\boldsymbol{P}_{T,k}^{-} = \boldsymbol{A}_{T,k-1}\boldsymbol{P}_{T,k-1}^{+}\boldsymbol{A}_{T,k-1}^{T} + Q_{T,k} \tag{20b}$$

$$K_{T,k} = \boldsymbol{P}_{T,k}^{-}\boldsymbol{C}_{T,k}^{T}(\boldsymbol{C}_{T,k}\boldsymbol{P}_{T,k}^{-}\boldsymbol{C}_{T,k}^{T} + R_{T,k})^{-1} \tag{20c}$$

$$\hat{\boldsymbol{x}}_{T,k}^{+} = \hat{\boldsymbol{x}}_{T,k}^{-} + K_{T,k}(y_{T,k} - \boldsymbol{C}_T \hat{\boldsymbol{x}}_{T,k}^{-} - \boldsymbol{D}_T u_{T,k}) \tag{20d}$$

$$\boldsymbol{P}_{T,k}^{+} = \left(\boldsymbol{I} - K_{T,k}\boldsymbol{C}_{T,k}\right)\boldsymbol{P}_{T,k}^{-} \tag{20e}$$

In the above iterations of the EKF algorithm, Equations (20a) and (20b) represent the time update of the internal temperature estimator, and Equations (20c), (20d) and (20e) represent the measurement update. In Equation (20), $K_{T,k}$ is the Kalman gain at the kth sampling point; $\hat{\boldsymbol{x}}_{T,k}^{-}$ and $\hat{\boldsymbol{x}}_{T,k}^{+}$ are the priori and posteriori estimates of the state matrix, which is initialized by $\hat{\boldsymbol{x}}_{T,0}^{+} = \mathrm{E}[x_{T,0}]$; $\boldsymbol{P}_{T,k}^{-}$ and $\boldsymbol{P}_{T,k}^{+}$ are the priori and posteriori estimates of the error covariance, which is initialized by $\boldsymbol{P}_{T,0}^{+} = \mathrm{E}[(x_{T,0} - \hat{\boldsymbol{x}}_{T,0}^{+})(x_{T,0} - \hat{\boldsymbol{x}}_{T,0}^{+})^T]$. With the help of the EKF algorithm and the results of the identification of thermodynamic parameters at small timescale, the battery T_{ia} at small timescale will be estimated with high accuracy. Further, in combination with the measurable ambient temperature T_{amb} value, the internal temperature T_i of the battery will be calculated under each moment.

It is worth stating that the parameters C_i and C_s, which characterize the thermal storage capacity, and R_i, which characterizes the thermal conductivity, depend on the properties of the material and remain essentially constant over the life of the cell. The value of R_s, which characterizes the heat transfer from the battery itself to the environment, is affected by certain external heat dissipation conditions, which have been studied in our previous work [13]. Considering that the test experiments used for data set acquisition in this paper are conducted in a constant temperature chamber with the same and stable thermal conditions, which makes the external thermal resistance R_s value almost constant. Therefore, the external thermal resistance R_s value is not considered separately to minimize the computational complexity of the multi-physics domain coupling modeling.

3.3 EKF-based capacity estimator development at large timescale

Given this fact that the decay of the available capacity over the entire life cycle is much smaller

than the variation in terminal voltage and internal temperature, it is reasonable and meaningful that a sub-observer for the estimation of the battery's current available capacity be developed on a larger timescale. As in the analysis of the time-scale design for slow kinetic parameters identification at small timescale above, the use of fixed-step for the design of time-scale under different timescale algorithms is also a natural solution. Similarly, the inability to adapt to all operating conditions is still a design drawback of this solution. In this paper, we also design an adaptive drive time-scale for performing the estimation of the available battery capacity at large timescale. First, according to the calculation law of the transferred charge, we can obtain the amount of charge change under current excitation as shown in Equation (21).

$$Q_{sum} = \sum_{k=0}^{l} \left| I_k \cdot \Delta t \right| \tag{21}$$

In Equation (21), Q_{sum} represents the sum of the absolute values of the battery transfer charge during time $k = 1{:}\,l$, and l represents the step size experienced by the capacity estimator during one execution, the value of which adaptively changes with the setting of the current excitation drive threshold. As suggested in the Ref. [42], we use $Q_{sum} > 0.12$ Ah to implement a driving threshold design for the available capacity estimator at large timescale. Specifically, during the operation of the battery embedded system, if the accumulated variation of the transferred charge is greater than 0.12 Ah, the instruction to execute the capacity estimation sub-algorithm will be sent. At the same time, the system will restart calculating the value of Q_{sum} until the next trigger threshold is met.

Under the premise that state-space equation for the aging characteristic sub-model is available, the EKF algorithm is chosen for battery capacity estimator development at large timescale. The simplicity of the EKF algorithm and the reliability of its use for capacity estimation have also been demonstrated in many Refs. [9,17,48]. First, we choose Q_{aged} as the state variable x_Q of the battery aging

characteristic sub-model. Meanwhile, the real-time SOC value of the AHC iteration considering the effect of the battery internal temperature is chosen as the output variable y_Q. Then, if we define:

$$h(SOC_k, I_k, x_{Q,k}) = SOC_k + \Delta t \cdot \eta_I \eta_T I_k / x_{Q,k} \tag{22}$$

Assuming that Equation (22) is derivable at all sample points, the first-order Taylor expansion is the observation matrix C_Q that can be used to calculate the aging characteristic sub-model, and the result is shown in Equation (23).

$$C_{Q,k} = \frac{\partial h(SOC_k, I_k, x_{aged,k})}{\partial x_{aged}}\Big|_{x_{aged}=\hat{x}^-_{aged,k}} = -\Delta t \cdot \eta_I \eta_T I_k / (Q_{aged,k})^2 \tag{23}$$

Further, the main iterative equation of the EKF-based capacity estimation sub-algorithm is shown in Equation (24).

$$\hat{x}^-_{Q,k} = \hat{x}^+_{Q,k-1} \tag{24a}$$

$$P^-_{Q,k} = P^+_{Q,k-1} + Q_{Q,k} \tag{24b}$$

$$K_{Q,k} = P^-_{Q,k} C^T_{Q,k} (C_{Q,k} P^-_{Q,k} C^T_{Q,k} + R_{Q,k})^{-1} \tag{24c}$$

$$\hat{x}^+_{Q,k} = \hat{x}^-_{Q,k} + K_{Q,k}(y_{Q,k} - h(SOC_k, I_k, \hat{x}^-_{Q,k})) \tag{24d}$$

$$P^+_{Q,k} = \left(I - K_{Q,k} C_{Q,k}\right) P^-_{Q,k} \tag{24e}$$

In the above iterations, Equations (24a) and (24b) represent the time update of the capacity estimator in the large time scale, and Equations (24c), (24d) and (24e) represent the measurement update. In Equation (24), $Q_{Q,k}$ and $R_{Q,k}$ are the covariances of w_Q and v_Q at k moments, respectively; $K_{Q,k}$ is the Kalman gain of the sub-algorithm in the capacity estimator; $\hat{x}^-_{Q,k}$ and $\hat{x}^+_{Q,k}$ are the prior and posterior estimates of the state matrix, respectively, which is initialized by $\hat{x}^+_{Q,0} = \mathrm{E}[x_{Q,0}]$; $P^-_{Q,k}$ and $P^+_{Q,k}$ are the prior and posterior estimates of the error covariance, respectively, which is initialized by $P^+_{Q,0} = \mathrm{E}[(x_{Q,0} - \hat{x}^+_{Q,0})(x_{Q,0} - \hat{x}^+_{Q,0})^T]$. The EKF-based capacity estimation sub-algorithm is executed when Q_{sum} reaches the set threshold of the system. Further, in combination with the AHC method in

the laboratory case where the initial value of SOC is known, the available capacity of the battery will be estimated with high accuracy at specific timescale.

3.4 Overall framework of the proposed AMTDIE strategy

In this section, decoupled identification of complex kinetic parameters based on quantification of time-scale differences and online state estimation of terminal voltage, internal temperature and available capacity at multiple timescales are implemented. Specifically, kinetic parameters decoupling identification, terminal voltage prediction, and online internal temperature estimation are performed on small timescale, while battery available capacity estimation is performed on large timescale. Also, the response times of the complex kinetic processes inside the cell are extracted and quantified for application to the decoupled identification of the model parameters. With the detailed development of the above four sub-observers with different functions, the whole framework of the proposed AMTDIE strategy is presented in Fig. 3.

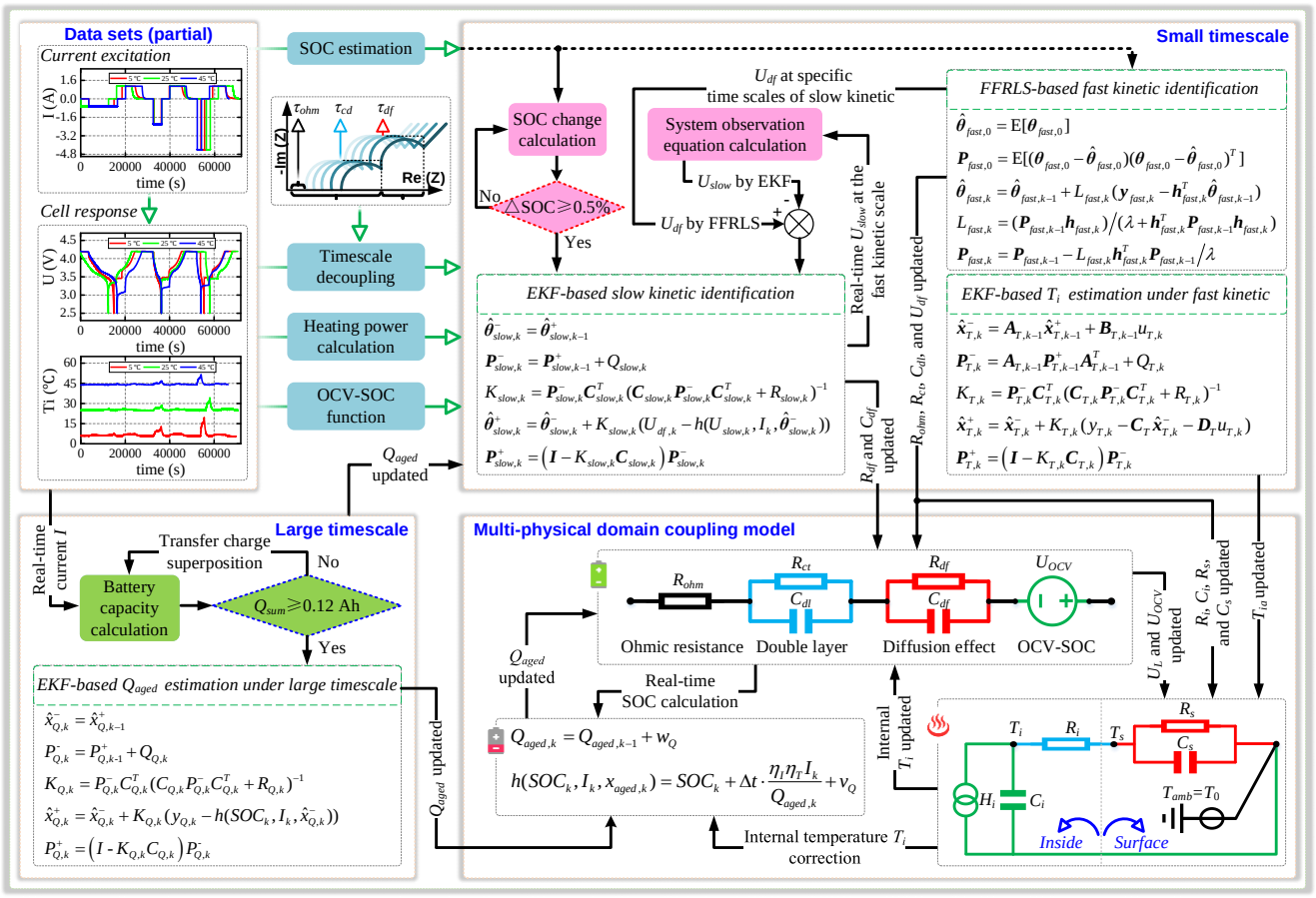

Fig. 3. Overall framework of adaptive multi-timescale decoupled identification and estimation strategy.

In Fig. 3, the time-scale design principles of the state estimator in different timescales and the iterative correction process of each sub-algorithm are shown. In small timescale, the FFRLS-based high-pass parameter discriminator under fast kinetic is executed under each sampling period, and the EKF-based low-pass parameter discriminator under slow kinetic is executed under a specific sampling period. Meanwhile, the online monitoring for the internal temperature is implemented by high-pass estimators based on the EKF algorithm under fast kinetic. In large timescale, the implementation of the battery available capacity estimator is realized by the EKF algorithm based on a specific time-scale driven design.

In addition, the execution of the high-pass parameter discriminator and the internal temperature estimator follows the basic timescale property under the system, and the execution of the low-pass parameter discriminator under the slow kinetic is controlled by the ΔSOC. Meanwhile, the execution of

the battery capacity estimator in the large timescale is controlled by Q_{sum}. By separating and designing the time-scales for driving different estimators, online parameter identification and state monitoring of battery MPDCM in different timescales are realized. It is not difficult to find that the above modeling strategy does not introduce additional variables. Meanwhile, the drivers under different timescales will reduce the computational complexity of the whole modeling to a certain extent, which in turn improves the efficiency of the whole system for online embedded applications.

4 Experiments and results analysis

4.1 Experimental platform and procedure

To verify the modeling accuracy of the lumped parameter MPDCM and the performance of the proposed AMTDIE strategy, an experimental platform consisting of equipment such as a mainframe, a temperature chamber and a battery test system, as shown in sub-Fig. 4(a), is constructed. Then, a new commercial NCM battery with model number HTCNR 18650 and the specific parameters shown in sub-Fig. 4(b) is chosen as the experimental sample. It should be noted that the electric-thermal-aging multi-physics domain coupling modeling method proposed in this paper is also applicable to other chemical types of batteries since they have similar external properties. Moreover, the battery pack level multi-physics domain coupling modeling work has not been made more detailed study in this paper. Given that the characteristics of the OCV-SOC relationship and the multi-timescale effects at the battery pack level are similar to those of the battery singletons, the modeling approach proposed in this paper is therefore also applicable to the battery pack level.

Further, the Compound ratio hybrid pulse power characteristic (CRHPPC) test at different temperatures (5, 25 and 45 ℃) is designed to ensure the reliability of the parameter identification. Also,

the Compound ratio constant current and constant voltage (CRCCCV) experiment at different temperatures and discharge ratio (0.3, 1.0 and 2.0 C) is designed to estimate the accuracy of the battery state. The work step flow of CRHPPC and CRCCCV testing is shown in sub-Fig. 4(c). In addition, three-dimensional data sets of OCV, SOC and internal temperature are available from the CRHPPC experimental results. Three-dimensional data sets of discharge ratio, available capacity, and internal temperature are available from CRCCCV condition. Moreover, the entropy heat coefficient is an important parameter in the multi-physics domain coupling modeling. In this work, the calculation of this value at different temperatures is achieved by using the OCV derivative with respect to temperature based on the selection of different SOC values at 11 equally spaced locations. The results of the above three-dimensional data set extraction are shown in sub-Fig. 4(d).

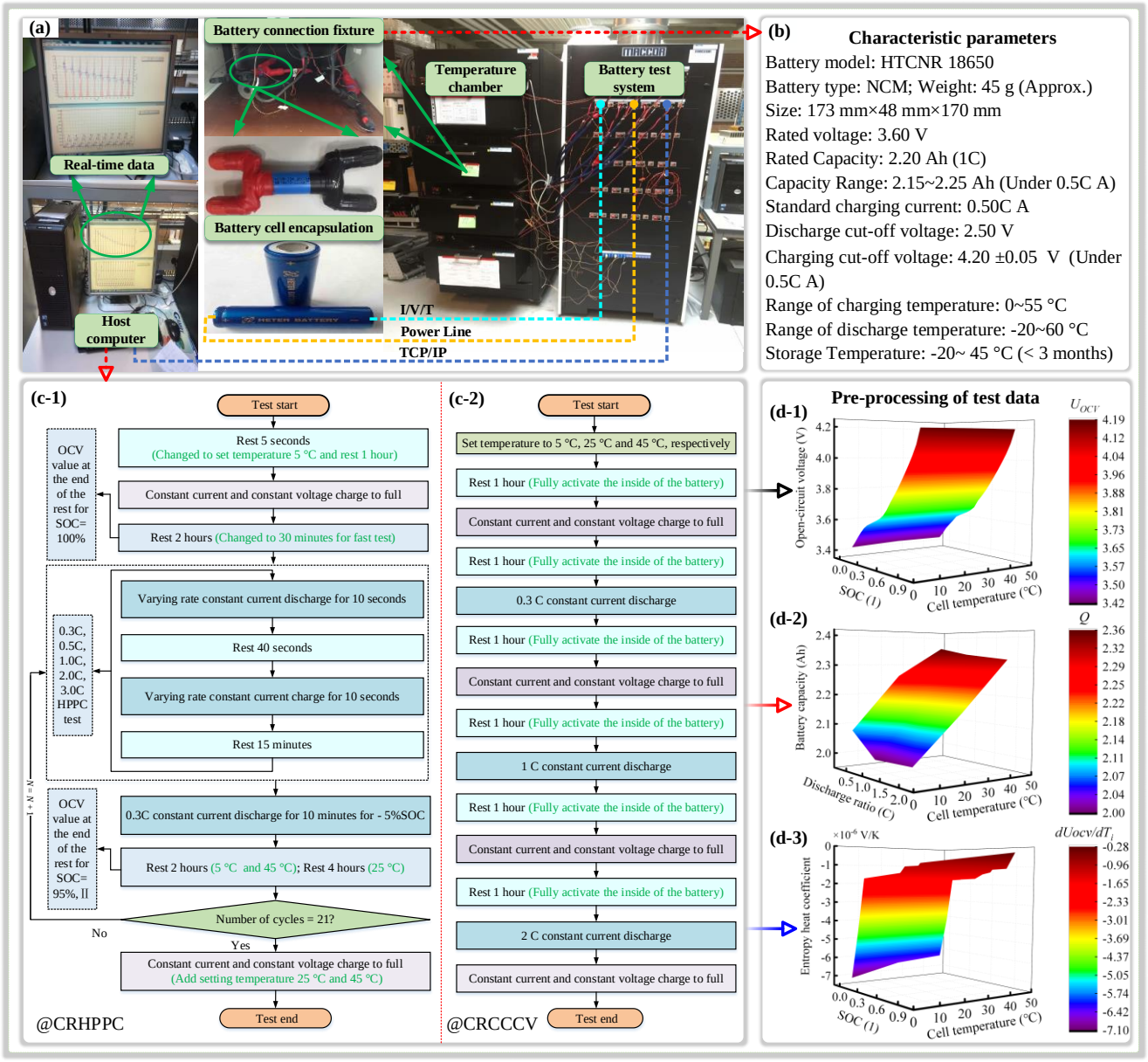

Fig. 4. Experimental platform and procedure: (a) Experimental platform; (b) Battery characteristic parameters; (c) Experimental procedure of CRHPPC and CRCCCV; (d) Three-dimensional data sets between different battery states.

With the support of the experimental platform, the acquisition of the battery temperature data in this paper is achieved by high-precision temperature sensing. Among them, the temperature sensor attached to the battery surface is used to measure the surface temperature, and the sensor fixed on the pole lug is used to obtain the temperature of the battery pole column. It is worth stating that a special electrical tape with adiabatic insulation is used for the sealing between the temperature sensor and the battery in all experiments of this paper. Benefiting from this treatment, battery pole temperature is

considered as the internal temperature and can be used to reflect the internal heat change of the battery under current excitation. With the aim of covering the operating temperature range (0 to 55 °C) of the battery samples as wide as possible, sufficient data sets are collected in this paper at 5 °C, 25 °C and 45°C, respectively. The experimental results and important information such as the time spent in each set of operating conditions are shown in Fig. 5.

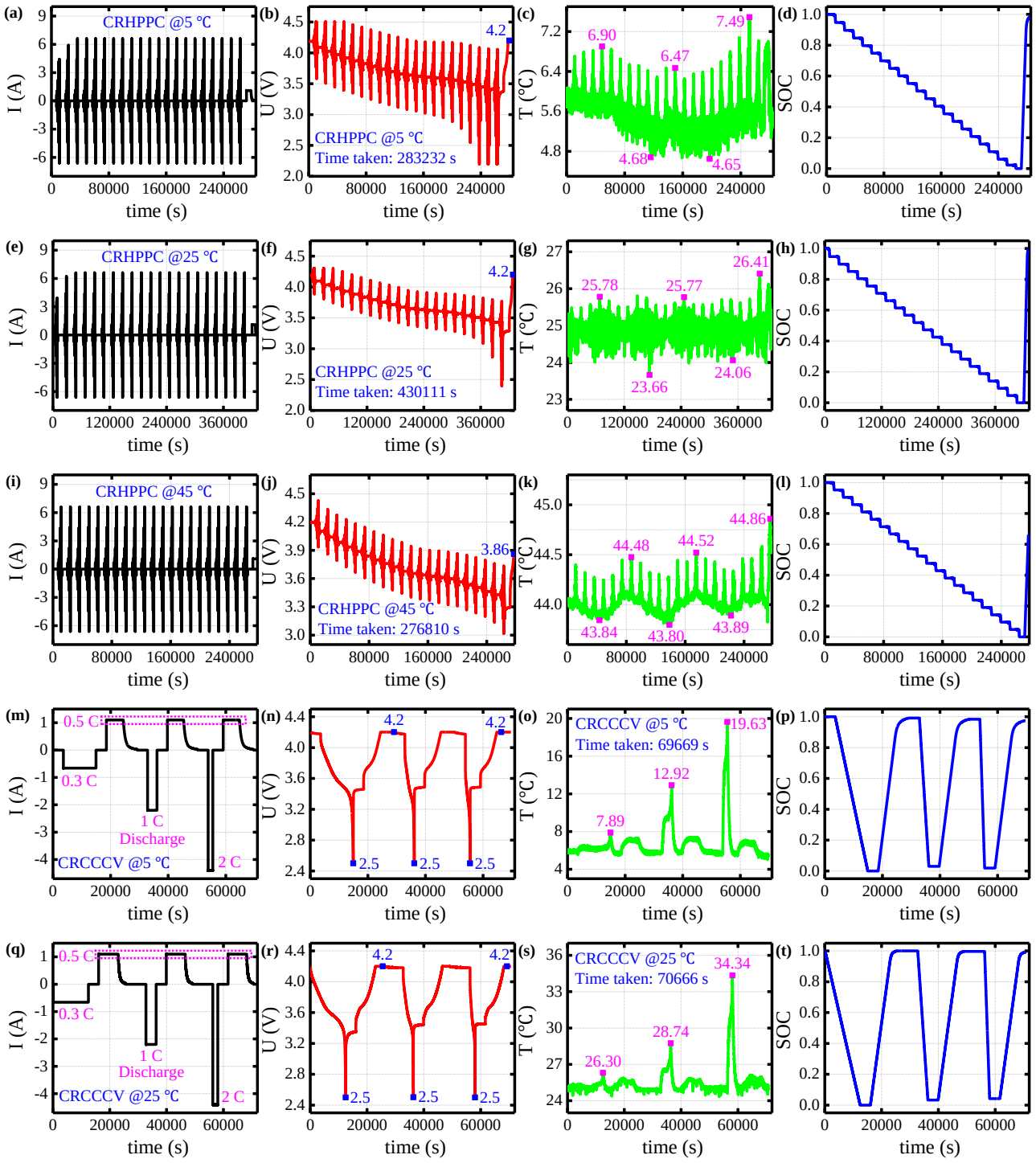

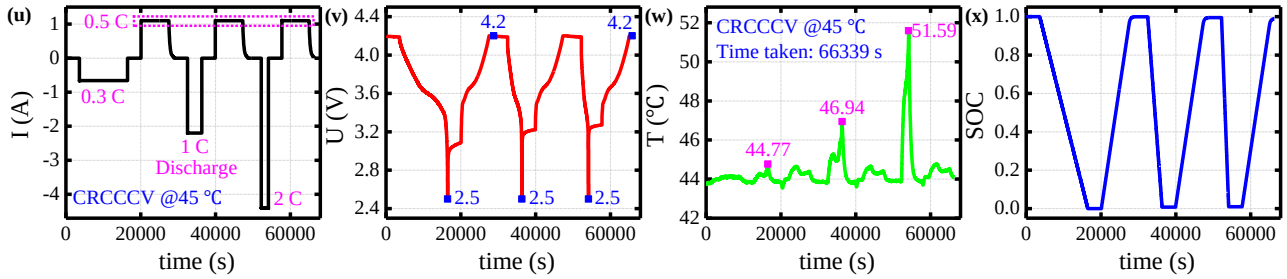

Fig. 5. Experimental results under different working conditions: (a-d) CRHPPC at 5 ℃; (e-h) CRHPPC at 25 ℃; (i-l) CRHPPC at 45 ℃; (m-p) CRCCCV at 5 ℃; (q-t) CRCCCV at 25 ℃; (u-x) CRCCCV at 45 ℃.

It is worth stating that the maximum charging current and the maximum continuous discharging current of the selected battery samples can reach 6.6 A. Therefore, in this paper, a pulse current of 3 C is included in the design of CRHPPC working condition. Meanwhile, under the premise of ensuring the safety of the battery, the upper safe voltage limit of the CRHPPC experiment is set to 4.5 V, and the lower safe voltage limit is set to 2.2 V. Under this fact, the terminal voltages greater than 4.2 V and less than 2.5 V appearing in Figs. 5(b), (f) and (g) are reasonable. The CRHPPC condition can greatly improve the simulation degree of the battery to the potential use environment. In addition, the CRHPPC condition can accelerate the aging of the battery under the premise of experimental safety, which greatly improves the efficiency of aging data collection. Another phenomenon that can be found from Figs. 5(b), (f) and (j) is that the CRHPPC working hours at 25 °C are about 40 hours longer than those at 5 °C and 45 °C. The main reason for this phenomenon is that in the CRHPPC experiments at 5 °C and 45 °C the resting time of the battery after each 5% reduction in SOC is 2 hours. In contrast, in the CRHPPC experiments at 25 °C the resting time of the battery is 4 hours, also as shown in Fig. 4(c-1). This design can support the validation of the effectiveness of the proposed algorithm.

4.2 Results of MPDCM-based identification of kinetic parameters

Based on the experimental results of CRHPPC and CRCCCV at different temperatures, the high-pass parameter discriminator based on the FFRLS algorithm under fast kinetic and the low-pass

parameter discriminator based on the EKF algorithm under slow kinetic are performed synergistically but separately within the small timescale of the proposed AMTDIE strategy. By combining the results of the three-dimensional data set shown in Fig. 4(d), the fast kinetic parameters R_{ohm}, R_{ct}, C_{dl}, R_{df} and C_{df} are identified under different time-scale driving. The identification results of all electrical characteristic parameters are shown in Fig. 6.

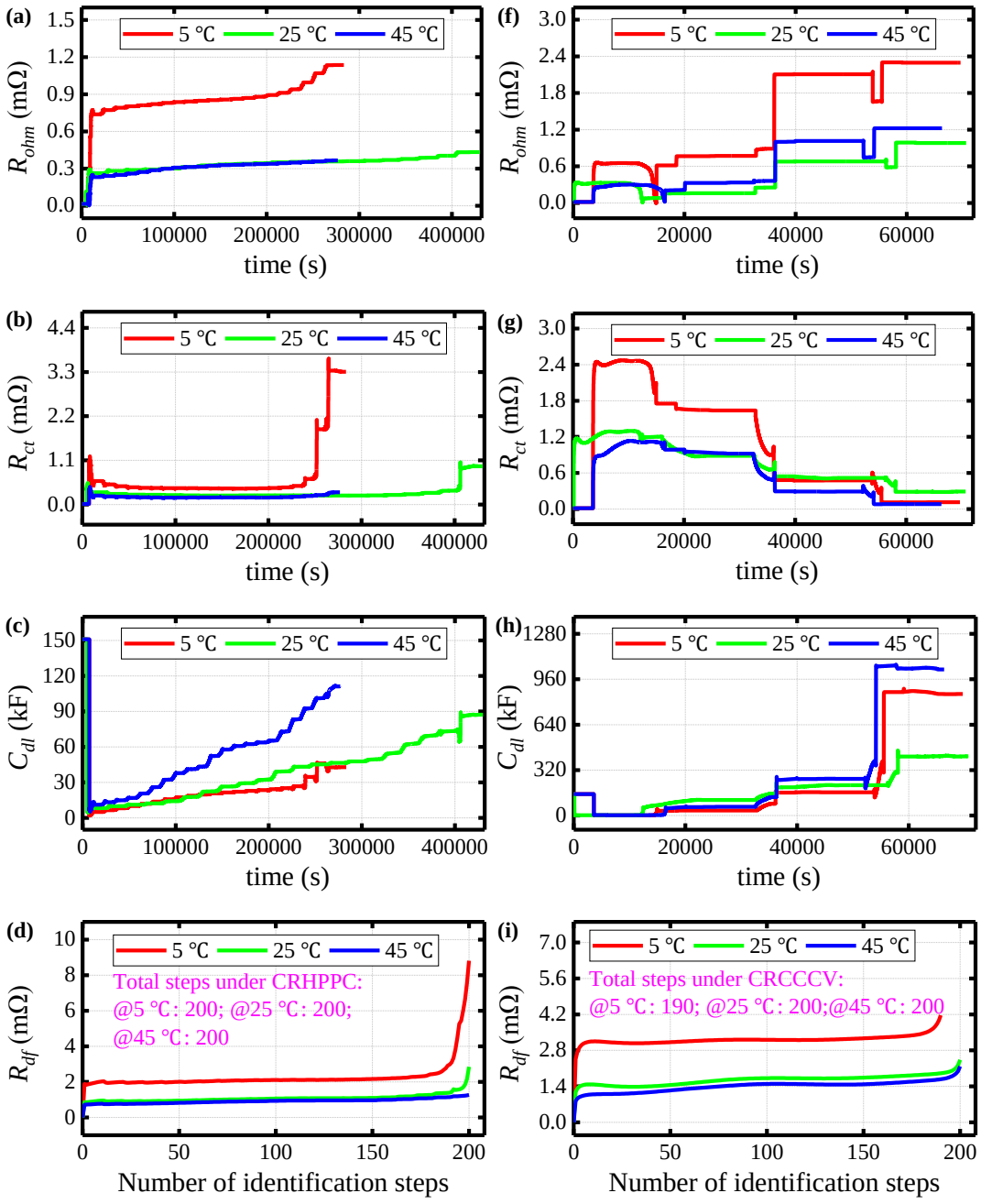

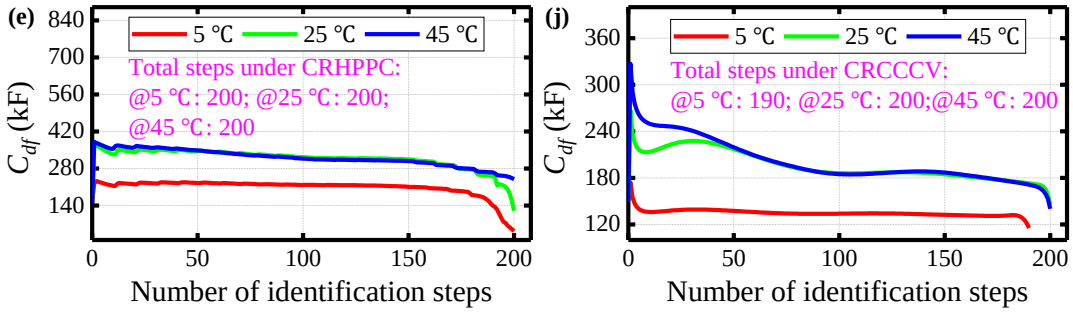

Fig. 6. Identification results of electrical characteristic parameters under different working conditions at different temperatures: (a-e) CRHPPC; (f-j) CRCCCV.

The Fig. 6 shows the result curves of the identification of the electrical characteristic parameters at different temperatures for the CRHPPC and CRCCCV operating conditions. It is clearly observed that the horizontal axis of the curve for the identification of the concentration difference polarization parameters in both operating conditions is not time in the traditional sense, but the number of identification steps. This is mainly due to the fact that the adaptive multi-timescale decoupling identification and estimation strategy actively distinguishes the fast and slow kinetic features inside the battery in small timescale. It can be observed in the sub-Figs. 6(a-e) that the iteration steps of R_{ohm}, R_{ct} and C_{dl} under fast kinetic at different temperatures are consistent with the total duration of the CRHPPC condition. Unlike the above case, the iteration steps of R_{df} and C_{df} are only related to the amount of SOC variation and are not affected by the sampling frequency and the length of the working condition. Also, the identification results of R_{df} and C_{df} under the CRCCCV condition in sub-Figs. 6(i-j) show the fact that the number of identification steps is different for different current excitations. These experimental results fully demonstrate the strong adaptiveness and generalization of the low-pass filter drive timescale to the system conditions.

In addition, the strong correlation of the model parameters with temperature in different physical domains is confirmed from the resulting curves in Fig. 6. Among them, the correlation of resistive parameters shows that R_{ohm}, R_{ct} and R_{df} decrease with the increase of temperature, and the

correlation of capacitive parameters shows that C_{dl} and C_{df} increase with the increase of temperature. This correlation is consistent with the experimental results in the Ref. [12,44], and also proves that the proposed strategy in this paper is well compatible with temperature. In addition, the increased values of R_{ohm}, R_{ct} and C_{dl} at the end of discharge for both operating conditions can also be observed from Fig. 6. A major reason is due to the less internal active matter at low charge, which also indicates that the MPDCM has a higher fidelity in modeling the complex kinetic processes inside the battery.

In addition to the above effective identification of the electrical characteristic parameters, the MPDCM also needs to identify the thermodynamic parameters at small timescale. As mentioned in Section **2**, the parameters C_i and C_s, which characterize the thermal storage capacity, and R_i, which characterizes the thermal conductivity, are dependent on the material properties of the cell and remain essentially constant in use. Additionally, the test experiments used for data set acquisition in this paper are conducted in a constant temperature chamber with the same and stable thermal conditions, which also makes the external thermal resistance R_s value almost constant. With the above conclusion, the average results of R_i, C_i, R_s and C_s obtained from the experimental data of CRHPPC and CRCCCV at different temperatures are 1.78 °C/W, 138.62 J/°C, 7.85 °C/W and 0.59 J/°C, respectively.

4.3 Modeling accuracy validation from the small timescale perspective

4.3.1 Verification of internal battery temperature estimation

In the problem of internal battery temperature monitoring, the open-loop transfer function estimation (OLTFE) method under the lumped parameter thermal path model is often used in battery embedded systems due to its simplicity. In order to verify the ability of the high-pass temperature estimator developed based on the EKF algorithm in the proposed AMTDIE strategy to track the battery

internal temperature, the OLTFE method is chosen to be used as a control group. Based on the data sets under CRHPPC and CRCCCV experiments and the results of the identification of thermodynamic parameters, the internal temperature of the battery is estimated under the OLTFE algorithm and the proposed AMTDIE strategy, respectively.

It should be noted that under laboratory conditions, the battery is started for the experiment after sufficient shelving and the heat transfer conditions in the temperature-controlled chamber are essentially constant. The initial temperature state of the battery in this case can be considered to be the same as the ambient temperature. Moreover, and the OLTFE method and the proposed AMTDIE strategy are iteratively estimated for the internal temperature of the battery with the same initial value as well as the heat exchange conditions, which excludes the influence of the OLTFE method by the initial value of the temperature and the external heat exchange conditions. With the help of the thermal parameter identification results, the estimated internal temperature of the cell at different temperatures in small timescale is shown in Fig. 7.

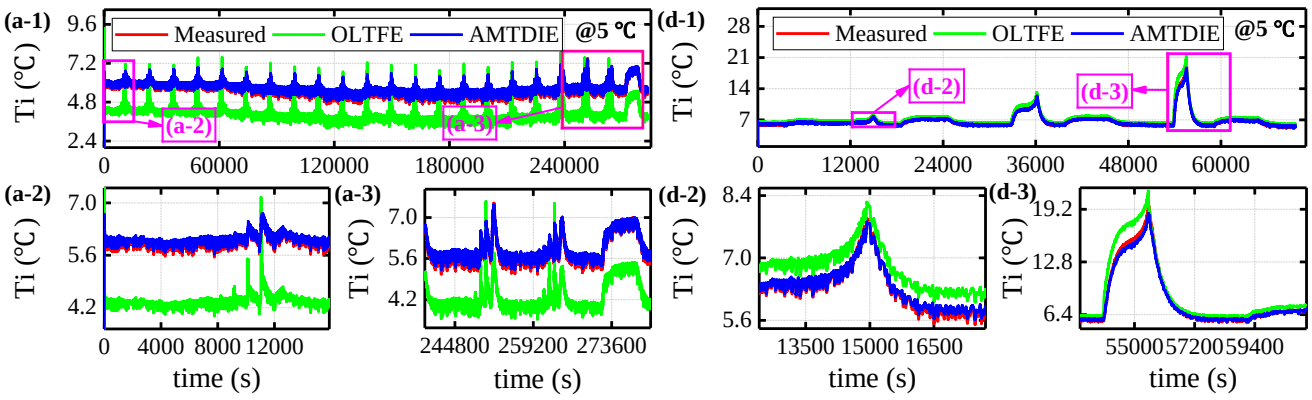

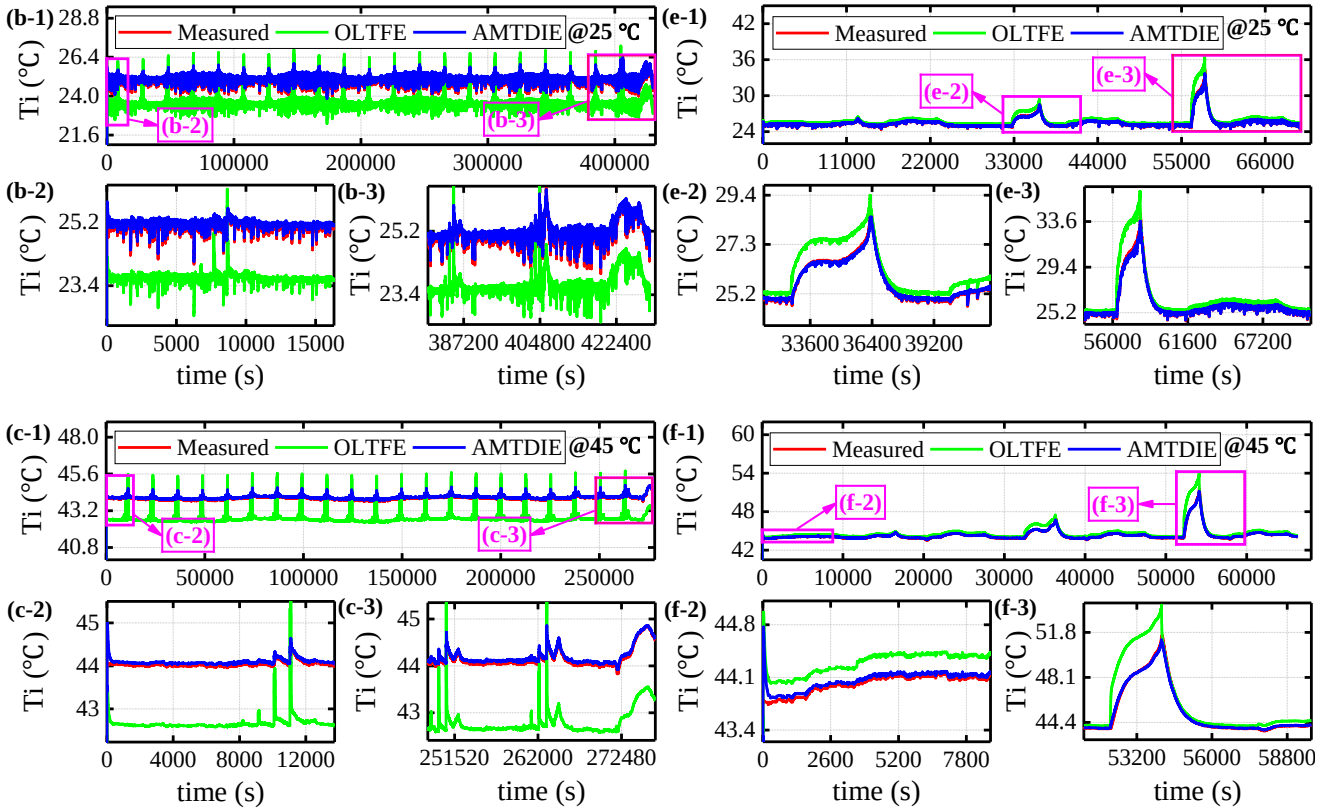

Fig. 7. Estimation results of internal temperature under different methods: (a) CRHPPC at 5 ℃; (b) CRHPPC at 25 ℃; (c) CRHPPC at 45 ℃; (d) CRCCCV at 5 ℃; (e) CRCCCV at 25 ℃; (f) CRCCCV at 45 ℃.

Sub-Figs. 7(a/b/c/d/e/f-1) shows the general overview of the tracking effect of the OLTFE method and the AMTDIE strategy on the battery internal temperature under CRHPPC and CRCCCV operating conditions at different temperatures. Sub-Figs. 7(a/b/c/d/e/f-2) and sub-Figs. 7(a/b/c/d/e/f-3) show the local enlargement of the internal temperature estimation curves. It can be observed from sub-Figs. 7(a/b/c/d/e/f-1) that both the OLTFE method as well as the proposed AMTDIE strategy can achieve effective tracking of the battery internal temperature. However, it can be clearly observed from sub-Figs. 7(a/b/c/d/e/f-2) and sub-Figs. 7(a/b/c/d/e/f-3) that the OLTFE method exhibits a large estimation error in the CRHPPC operating condition where the current direction transition frequency is fast. Compared to the OLTFE method, the EKF-based high-pass temperature estimator developed in the proposed AMTDIE strategy eliminates most of the estimation error with offset error from the results shown in Fig. 7. To show the estimation effect of the two methods more visually, the absolute error between the

estimated and measured values of the battery internal temperature is calculated as shown in Fig. 8.

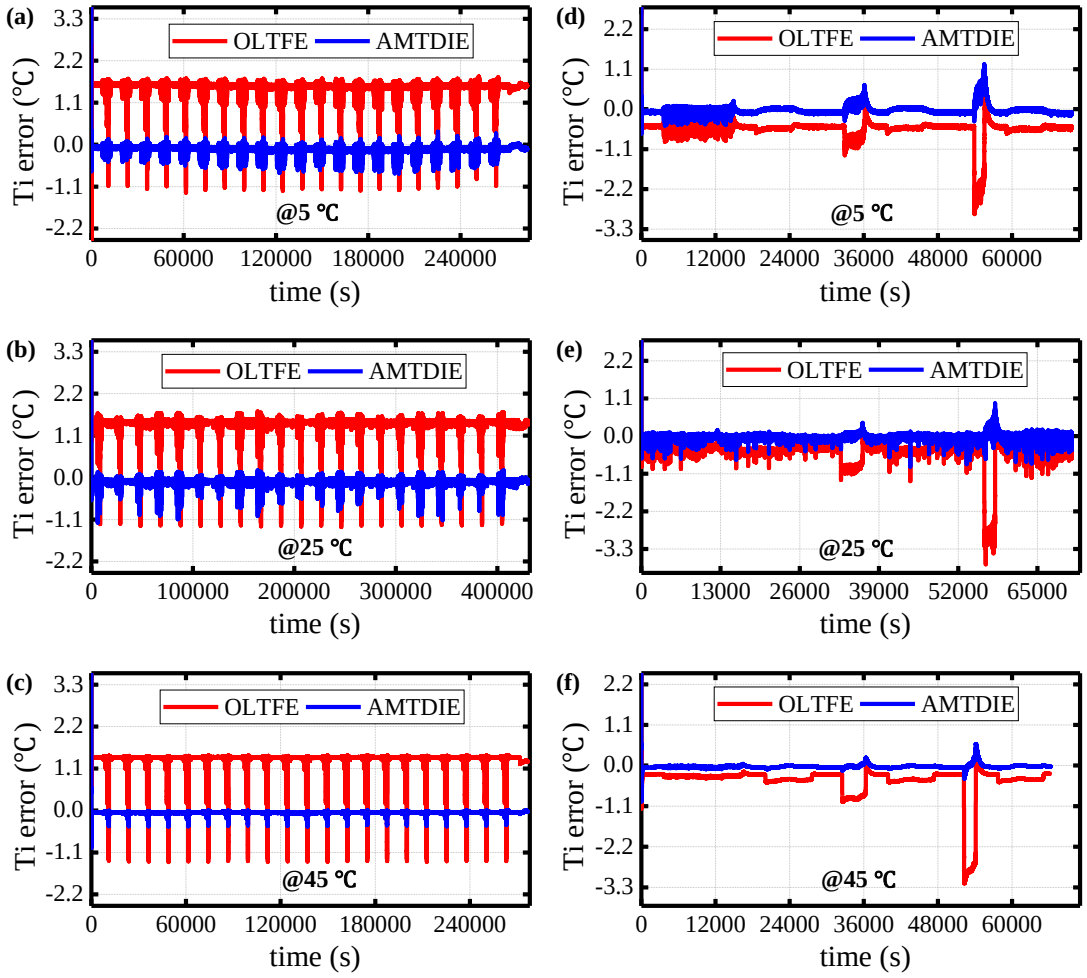

Fig. 8. Estimation errors of internal temperature under different methods: (a) CRHPPC at 5 ℃; (b) CRHPPC at 25 ℃; (c) CRHPPC at 45 ℃; (d) CRCCCV at 5 ℃; (e) CRCCCV at 25 ℃; (f) CRCCCV at 45 ℃.

From the absolute error curves of the two methods shown in Fig. 8, it can be observed that the internal temperature estimation error based on the proposed AMTDIE strategy is significantly lower than that of the OLTFE method. Comparing the error curves of the two methods under different working conditions, it is found that the AMTDIE strategy has better performance in the CRHPPC working condition with faster current direction switching frequency and the CRCCCV working condition with constant current long-time charging and discharging, especially in the CRCCCV working condition. A major reason is that the EKF-based high-pass temperature estimator in the proposed AMTDIE strategy is the logic of the closed-loop mechanism. During the iteration of the algorithm, the Kalman gain $K_{T,k}$

in the high-pass temperature estimator can quickly adapt to the temperature fluctuation error caused by the current commutation. This allows the algorithm to exhibit a stronger feedback correction capability, thus ensuring the accuracy of the internal temperature estimation, which is a fundamental difference from the OLTFE method. In addition, the OCV and terminal voltage values optimized based on the actual capacity are coupled in the internal battery heating power equation, which is also contributing to the excellent internal temperature estimation under the AMTDIE strategy. Further, four quantitative indexes of root-mean-square error (RMSE), mean absolute error (MAE), mean absolute percentage error (MAPE) and maximum error (ME) under different operating conditions are calculated in this paper for analyzing the performance of the proposed AMTDIE strategy on the internal temperature estimation of the battery. The detailed formula for each index can be found in Ref. [17,33], and the calculation results are shown in Fig. 9.

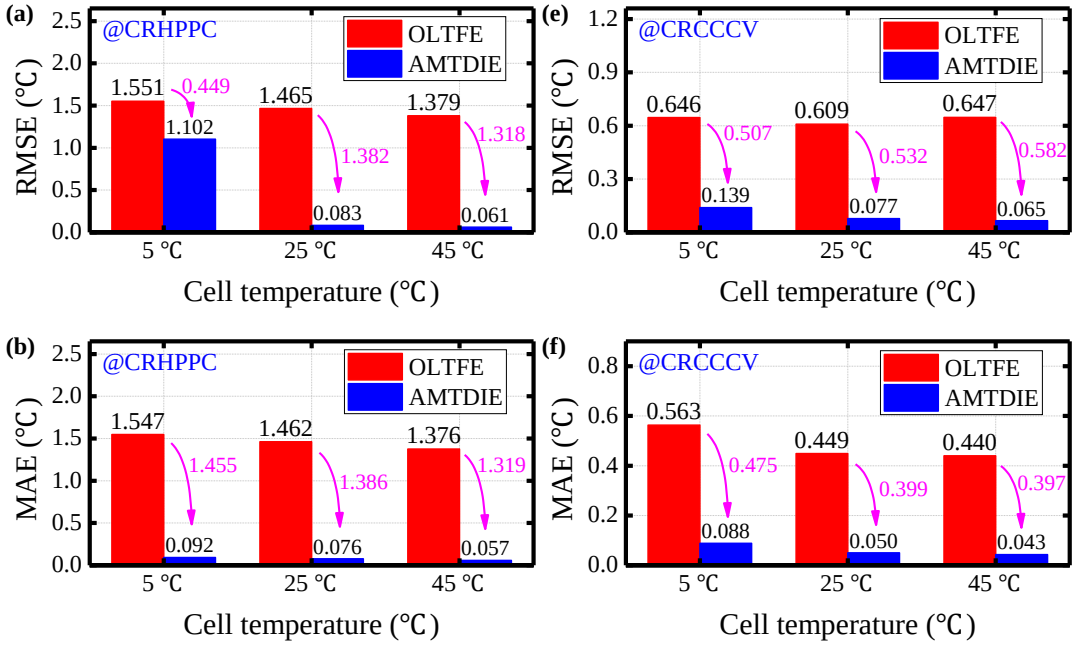

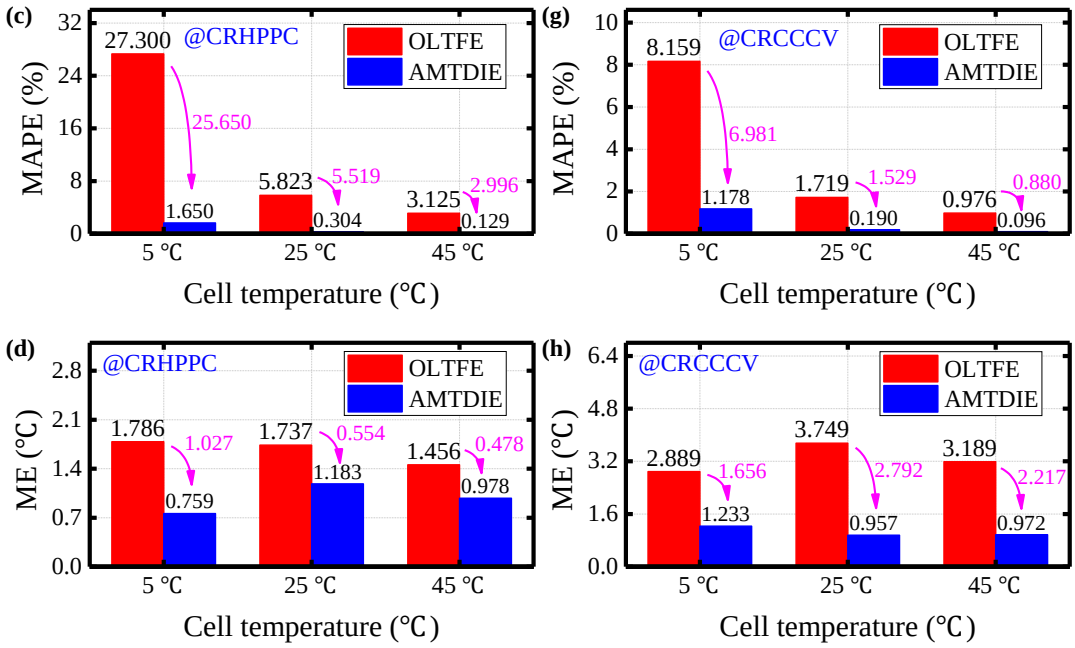

Fig. 9. Results of each quantitative index for internal temperature estimation under different methods: (a) RMSE under CRHPPC; (b) MAE under CRHPPC; (c) MAPE under CRHPPC; (d) ME under CRHPPC; (e) RMSE under CRCCCV; (f) MAE under CRCCCV; (g) MAPE under CRCCCV; (h) ME under CRCCCV.

Observing the calculation results of each quantitative index shown in Fig. 9, it can be found that the RMSE, MAE, MAPE and ME based on the proposed AMTDIE strategy are reduced by 0.449 °C, 1.319 °C, 2.996% and 0.487 °C under CRHPPC conditions at 5, 25 and 45 °C, respectively, compared with the OLTFE method. Under CRCCCV conditions, the RMSE, MAE, MAPE and ME indexes based on the proposed strategy were reduced by a minimum of 0.507 °C, 0.397 °C, 0.880% and 1.656 °C, respectively. In addition, the maximum error of the internal temperature based on the OLTFE method under CRHPPC and CRCCCV is 1.786 °C and 3.749 °C, respectively, due to the lack of closed-loop correction mechanism. By comparison, the ME of the internal temperature estimation based on the proposed strategy is reduced from 0.478 °C to 1.027 °C and from 1.656 °C to 2.792 °C ranging from the OLTFE method, respectively.

In addition, compared with the fractional order electro-thermal coupling model based on electrochemical impedance poo in the literature [42] (the MAE of internal cell temperature prediction at

5, 25 and 45 °C are 0.602, 0.334 and 0.221°C, respectively), the algorithms proposed in this study improve the accuracy of the internal temperature estimation by a minimum of 0.510, 0.258, and 0.164°C, respectively, at the corresponding experimental temperatures. From these values, we can confirm that the proposed AMTDIE strategy has strong effectiveness and high accuracy in internal temperature estimation. In addition, observation from Fig. 9 also reveals that each quantitative index based on the OLTFE method at 5 °C is greater than that at 25 °C and 45 °C. The proposed AMTDIE strategy does not show this situation while improving the performance of the internal temperature estimation. This also proves that the proposed strategy can eliminate the effect of ambient temperature on the internal temperature estimation of the battery.

4.3.2 Verification of terminal voltage tracking effect

In order to verify the tracking effect of the proposed AMTDIE strategy on the battery terminal voltage, the FFRLS algorithm with fixed timescale is selected as the control group in this paper. Similarly, based on the data sets under CRHPPC and CRCCCV operating conditions, the prediction of the battery terminal voltage is performed under the FFRLS algorithm with fixed timescale and the AMTDIE strategy with quantization of timescale information, respectively. In order to increase the comparability of experimental results, the initialization conditions at iteration are the same for both algorithms. The different condition is that the proposed AMTDIE strategy has a real-time correction of the internal temperature as well as the available capacity to the terminal voltage in the battery electrical characteristic modeling due to the coupling of three important characteristics. With the electrical characteristic parameters effectively identified, the battery terminal voltage prediction results based on the AMTDIE strategy are shown in Fig. 10.

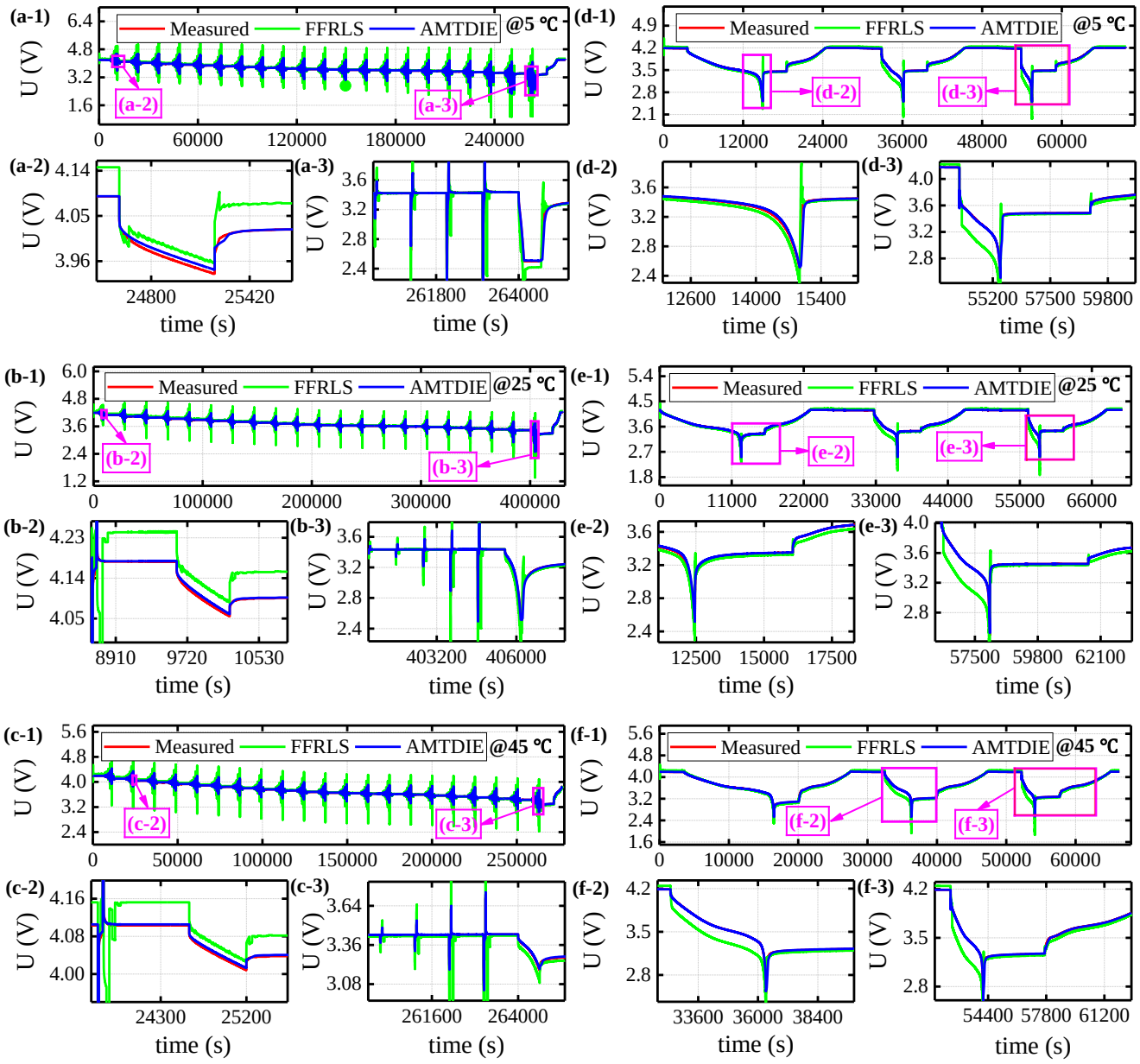

Fig. 10. Prediction results of terminal voltage under different methods: (a) CRHPPC at 5 ℃; (b) CRHPPC at 25 ℃; (c) CRHPPC at 45 ℃; (d) CRCCCV at 5 ℃; (e) CRCCCV at 25 ℃; (f) CRCCCV at 45 ℃.

Fig. 10 shows the tracking effect of the FFRLS algorithm at fixed timescale and the AMTDIE strategy considering complex kinetic response time factors on the battery terminal voltage. Among them, sub-Figs. 10(a-c) show the predicted results for CRHPPC condition at 5, 25 and 45 °C, respectively, and sub-Figs. 10(d-f) show the predicted results for CRCCCV condition, respectively. It can be observed that the estimated values of the battery terminal voltage based on the proposed AMTDIE strategy are closer to the true values than the FFRLS method based on the fixed timescale.

In comparison, the advantages of the proposed AMTDIE strategy are mainly reflected in two points. First, the estimation error of the terminal voltage due to the frequent current transition direction can be effectively corrected in time in the CRHPPC condition. In addition, the slow voltage change process due to the concentration difference polarization is effectively simulated in the CRCCCV condition, thus improving the prediction accuracy of the terminal voltage. In order to show the estimation effect of the battery terminal voltage more intuitively, the absolute errors of the two algorithms at small timescale are calculated and the results are shown in Fig. 11.

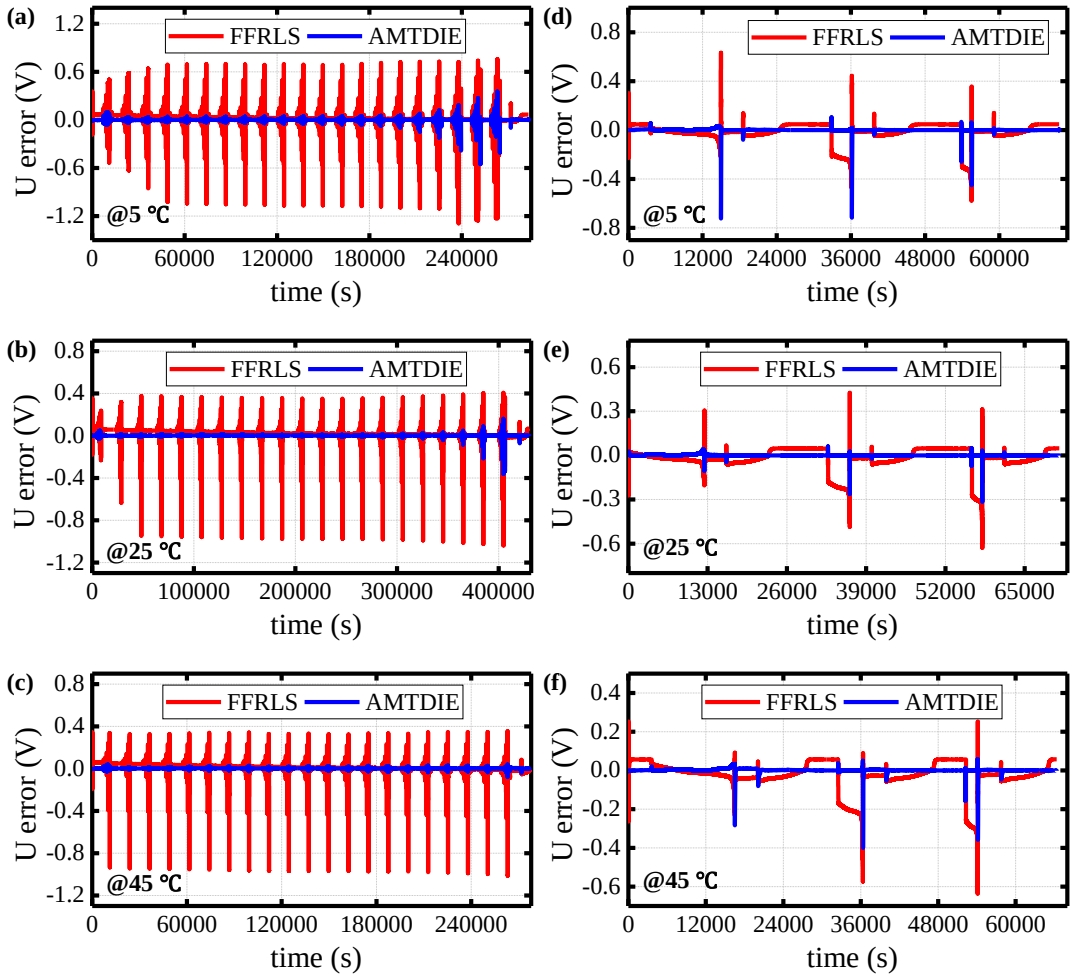

Fig. 11. Prediction errors of terminal voltage under different methods: (a) CRHPPC at 5 ℃; (b) CRHPPC at 25 ℃; (c) CRHPPC at 45 ℃; (d) CRCCCV at 5 ℃; (e) CRCCCV at 25 ℃; (f) CRCCCV at 45 ℃.

It can be visualized from Fig. 11 that the estimation error of the battery terminal voltage under the proposed AMTDIE strategy is smaller than that of the FFRLS algorithm at fixed timescale for almost

the whole iterative phase. Among them, the main reason for the reduction of the estimation error during constant-current charging and discharging is due to the fact that the parameters of the complex kinetic processes inside the battery are decoupled by the independent filter design, which is particularly evident in the CRCCCV condition shown in sub-Figs. 11(d-f). In addition, the terminal voltage estimation error at current direction transition is greatly improved with the proposed AMTDIE strategy compared to the FFRLS algorithm at fixed timescale. This effectively illustrates that the high-pass sub-filter in the proposed AMTDIE strategy can well capture the ohmic polarization and the concentration difference polarization processes under the fast kinetics inside the battery, which in turn reduces the battery terminal voltage prediction error during the current direction transition to some extent.

It is worth noting that there is a large error in the battery terminal voltage under both the proposed AMTDIE strategy and the traditional fixed timescale method when the battery SOC is low, which is more prominent under low temperature condition. This is mainly due to the fact that the battery exhibits high nonlinear characteristic when it is at low SOC, which brings errors to the acquisition of the battery OCV. In fact, due to the addition of the consideration of internal temperature as well as aging factors in the multi-physics domain coupled model in this paper, the above-mentioned terminal voltage estimation error at low SOC is also greatly eliminated. Further, the four quantitative indicators of RMSE, MAE, MAPE and ME for the terminal voltage estimation under different operating conditions are calculated in this paper and the results are shown in Fig. 12.

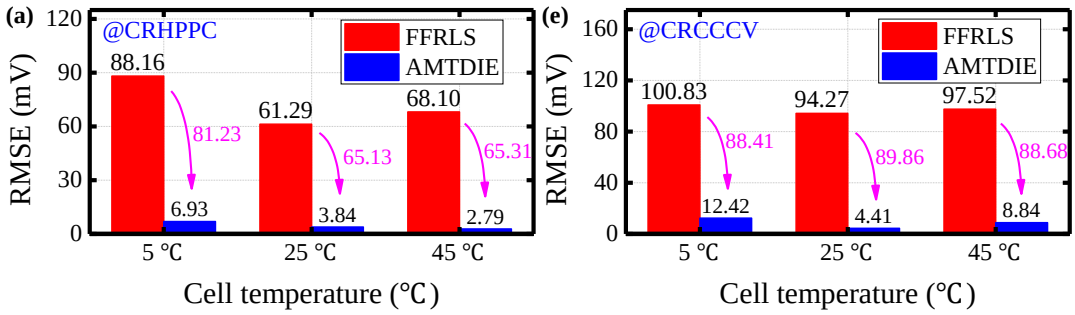

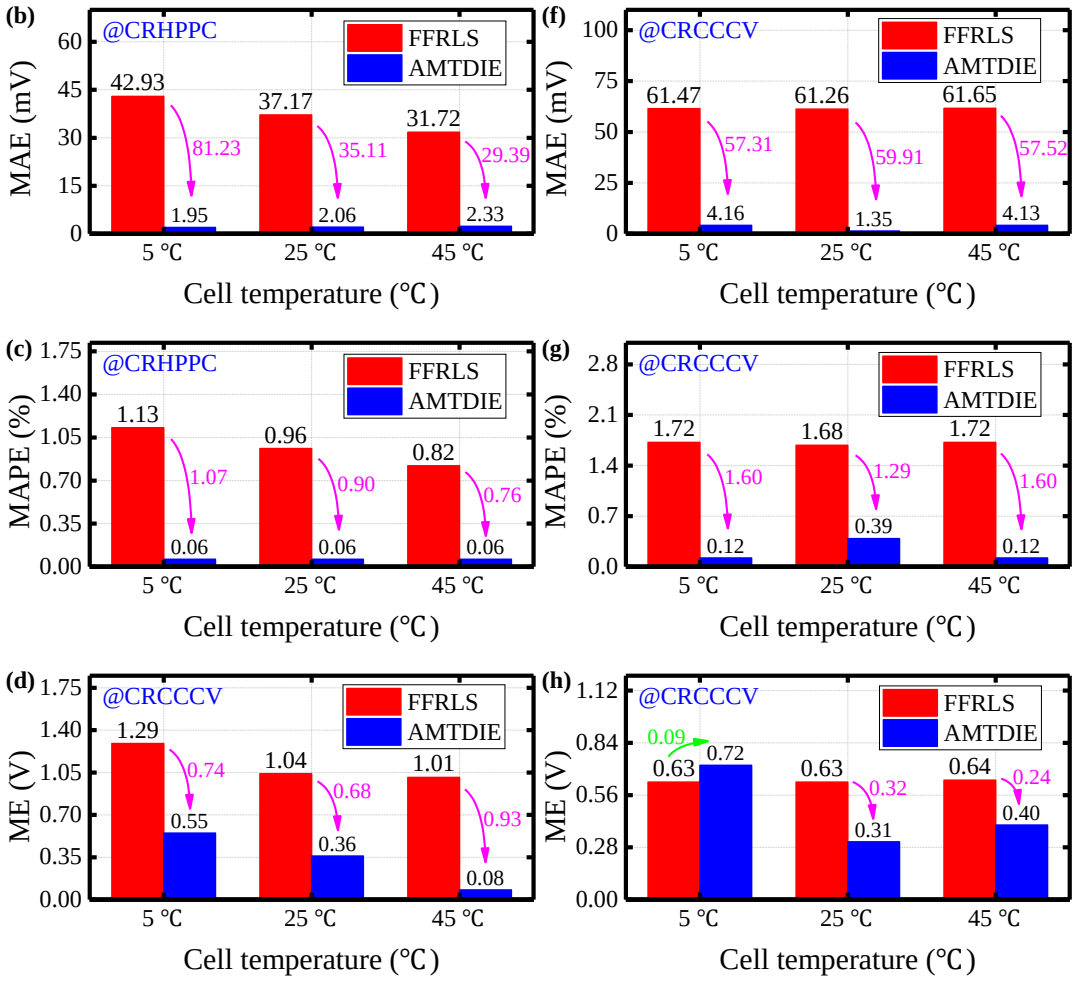

Fig. 12. Results of each quantitative index for terminal voltage prediction under different methods: (a) RMSE under CRHPPC; (b) MAE under CRHPPC; (c) MAPE under CRHPPC; (d) ME under CRHPPC; (e) RMSE under CRCCCV; (f) MAE under CRCCCV; (g) MAPE under CRCCCV; (h) ME under CRCCCV.

It can be found from Fig. 12 that the RMSE, MAE, MAPE and ME based on the proposed AMTDIE strategy have a maximum reduction of 89.86 mV, 81.23 mV, 1.60% and 0.93 V, respectively, compared to the traditional FFRLS method at fixed timescale under CRHPPC and CRCCCV operating conditions at different temperatures. In the low-temperature environment, the FFRLS based on a fixed timescale has a maximum RMSE of 100.83 mV and a maximum ME of 1.29 V after convergence of the algorithm. This error is not negligible for the battery with a nominal voltage of 3.60 V. Under the same low-temperature conditions, the RMSE and ME of the terminal voltage estimation based on the proposed AMTDIE strategy are 12.42 mV and 0.72 V, respectively. In addition, the proposed method in this study

improves the terminal voltage prediction accuracy by 11.38 mV compared to the three-dimensional state electrochemical-thermal coupling model based on electrochemical mechanism (the RMSE of terminal voltage prediction at room temperature is 23.8 mV) in literature [41]. Meanwhile, the proposed method in this study improves the terminal voltage prediction accuracy by 115.78 mV compared to the set-parameter based electro-thermal coupling model (the RMSE of terminal voltage prediction at room temperature is 128.2 mV) in the literature [45]. This figure proves that the proposed AMTDIE strategy has stronger temperature generalization than the FFRLS method at fixed timescale.

It is worth stating that the ME value of the terminal voltage error based on the FFRLS method is slightly smaller than the proposed AMTDIE strategy under the CRCCCV condition at 5 °C. Combining with sub-Fig. 12(d), it can be found that the errors before and after this voltage estimation point are less than 0.20 V. Therefore, we conjecture that the occurrence of this chance case is caused by the system error. At the same time, the significantly reduced RMSE, MAE, and MAPE calculations based on different methods for the CRCCCV condition at 5 °C also provide sufficient evidence for this conjecture.

4.4 Validation of available capacity estimates at large timescale

As part of the electrical-thermal-aging multi-physics coupled domain modeling, accurate estimation of the available capacity is important for predicting the battery terminal voltage and internal temperature. For the electrical characteristic sub-model in the multi-physics domain coupling modeling, the accurate battery available capacity can be used to correct the SOC values based on the AHC method and thus improve the accuracy of the OCV as well as the terminal voltage prediction. Meanwhile, the OCV and the terminal voltage, which are the inputs of the thermal characteristic sub-model, their highly accurate iterative results will improve the accuracy of the calculation of the battery heating power and thus guarantee the accuracy of the estimation of the battery internal temperature. With the feedback correction

of this coupling mechanism, the real-time available capacity estimation becomes more essential. Naturally, there are large timescale differences in the decay of battery capacity with respect to changes in terminal voltage and internal temperature. Based on this, the EKF-based battery available capacity estimator coupled in the AMTDIE strategy is developed at large timescale, which is driven by independent time-scale. To verify the effectiveness and accuracy of the proposed strategy, the experimental data sets of CRHPPC and CRCCCV at different temperatures are applied on in the battery available capacity estimation, and the results are shown in Fig. 13.

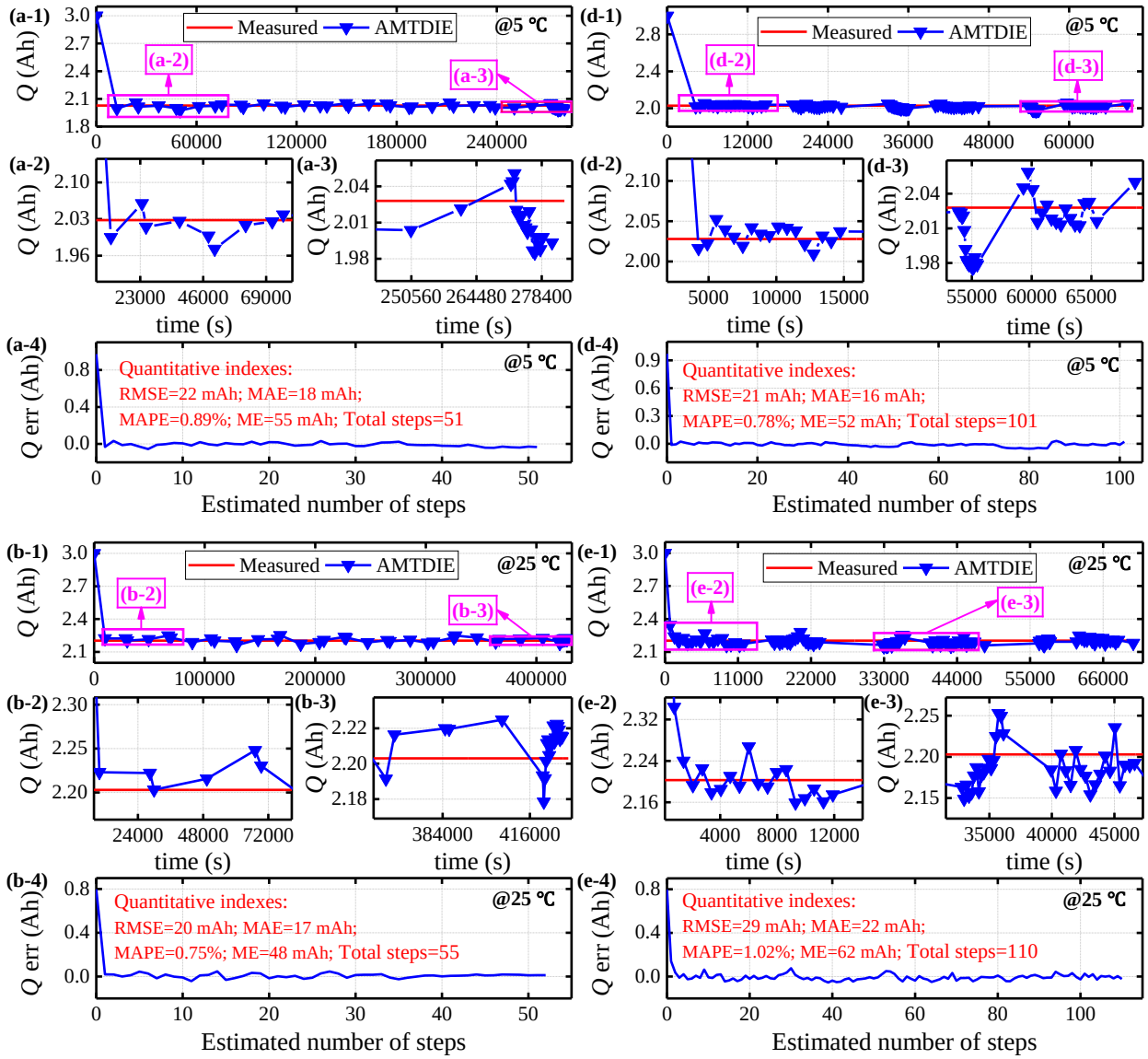

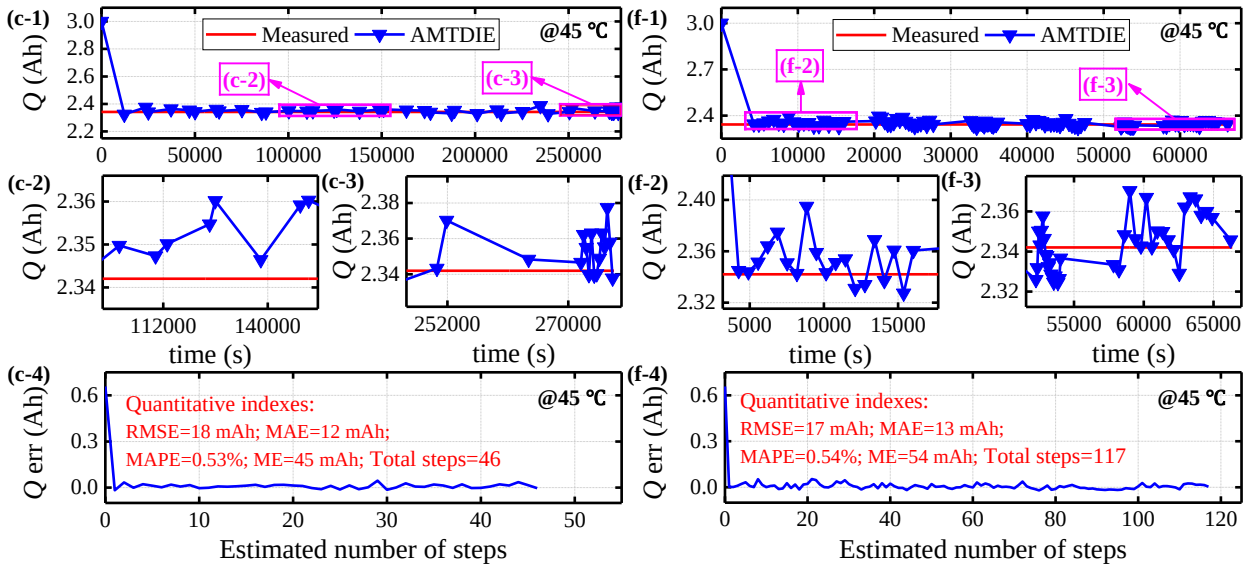

Fig. 13. Estimation results and errors of battery available capacity: (a) CRHPPC at 5 ℃; (b) CRHPPC at 25 ℃; (c) CRHPPC at 45 ℃; (d) CRCCCV at 5 ℃; (e) CRCCCV at 25 ℃; (f) CRCCCV at 45 ℃.

Fig. 13 shows the results of the battery available capacity estimation and each quantitative index. First, the capacity of the selected new battery sample is measured and the results show the actual available capacity at 5, 25 and 45 °C as 2.082, 2.203 and 2.342 Ah, respectively. Throughout the iterative process, the initialization of the capacity estimator at large timescale is chosen as 3 Ah with a large deviation from the actual battery capacity. From the estimation results of the battery available capacity, the convergence of the algorithm is achieved in the second iteration of the large timescale steps, except for the CRCCCV condition at 25 °C where the algorithm converges in the third iteration of the large timescale steps. This demonstrates the high convergence of the capacity estimator developed based on the EKF algorithm. In addition, from the calculated results of each quantitative index shown in Sub-Figs. 13(a/b/c/d/e/f-4), the maximum RMSE, MAE, MAPE and ME of the capacity estimation errors for CRHPPC condition at different temperatures are 22 mAh, 18 mAh, 0.89% and 55 mAh, respectively, and the maximum RMSE, MAE, MAPE and ME for CRCCCV condition at different temperatures are 29 mAh, 22 mAh, 1.02% and 62 mAh, respectively. These values strongly demonstrate the high accuracy of the capacity estimator in the AMTDIE strategy for large timescale.

More importantly, a particularly important phenomenon can be observed in sub-Figs. 13 (a/b/c/d/e/f-4), where the number of iteration steps of the proposed AMTDIE strategy on the available capacity estimation is only between 46 and 117, despite the fact that the total experimental time for both CRHPPC and CRCCCV conditions at different temperatures is between 18 and 120 hours. This is mainly due to the fact that the time-scale design at large timescale allows the capacity estimator to be executed only when usable Q_{sum} innovation is acquired. In the same way as the idea of slow kinetic parameters identification at small timescale, a separate adaptive time-scale driver can greatly reduce the computational complexity of AMTDIE strategy and improve the computational efficiency of the multi-physics domain coupling modeling. In addition, the intervals of any two consecutive capacity estimation steps are different, which reflects the basic principle of adaptive time-scale design at large timescale.

As a performance comparison of the proposed strategy, the large timescale capacity estimator based on recursive total least squares (RTLS) developed in the Ref. [49], which takes into account the effect of current offset error, is chosen as the control group. In order to reduce the influence of temperature on the battery capacity estimation and to ensure the validity and fairness of the control group as much as possible, we choose the above-mentioned literature NEDC operating conditions at 25 °C for comparison with the CRHPPC and CRCCCV operating conditions at 25 °C in this paper. The results show that the maximum relative error of capacity after convergence is 3.67% for the NEDC condition at 25 ℃ in the above-literature, and the maximum relative errors of capacity after convergence are 2.18% and 2.81% for the CRHPPC and CRCCCV conditions at 25 ℃ in this paper, respectively. In comparison, the proposed AMTDIE strategy in this paper has a slight improvement in accuracy. This also provides support for the effectiveness and accuracy of the large timescale capacity estimator developed based on the EKF algorithm in the proposed AMTDIE strategy.

5 Conclusions

Timescale based analysis provides sufficient and effective information to separate the kinetic behavior of the coupling inside the cell. In this paper, the complex kinetic processes inside the battery are decoupled by quantized time-scale features, and the modeling of the coupled electrical, thermal and aging multi-physical domains is realized in the form of lumped parameters. Meanwhile, an efficient adaptive multi-timescale decoupled identification and estimation strategy is proposed to realize the nondestructive characterization of the battery impedance and the online monitoring of the state characteristics.

Experimental results at 5, 25 and 45 °C for CRHPPC and CRCCCV conditions show that the proposed strategy has fast convergence and reliable accuracy for the characterization of complex kinetic parameters and the detection of different state properties. Among them, the RMSE, MAE, MAPE and ME indexes of internal temperature estimation at small timescale are controlled in the ranges of 0.061~1.102 °C, 0.043~1.092 °C, 0.096~1.650% and 0.759~1.183 °C, respectively, and the indexes of terminal voltage are controlled in the ranges of 2.79~12.42 mV, 0.06~0.39 mV and 0.08~0.72 mV, respectively. The estimates of battery usable capacity errors on large timescales are controlled within the ranges of 17-29 mAh, 12-22 mAh, 0.53-1.02%, and 45-62 mAh, respectively. Quantitative timescale characterization can provide new insights into the kinetic behavior inside decoupled batteries, especially for next-generation battery systems.

However, interface evolution and other unknown kinetic processes are not explored in detail in this study. In future work, we will focus our research on the acquisition of more valuable timescale information, which will in turn improve the time-scale identification decoupling and multi-physics domain coupling modeling of complex kinetic processes in batteries. Meanwhile, conducting full life

cycle aging experiments and simulation analysis for battery life modeling based on the data set is also one of the main future works.

Acknowledgments

This work is supported by the National Natural Science Foundation of China (Grant No. 62173281, 51975319, and 61801407) and the State Key Laboratory of Tribology and Institute of Manufacturing Engineering at Tsinghua University. To our co-author, Prof. Carlos Fernandez of Robert Gordon University, we appreciate your support. The authors would also like to thank Prof. D.-I. Stroe at Aalborg University for reviewing & editing.

References

[1] Hu X, Xu L, Lin X, et al. Battery lifetime prognostics. *Joule*, **2020**, 4(2): 310-346.

[2] Moy K, Lee S B, Harris S, et al. Design and validation of synthetic duty cycles for grid energy storage dispatch using lithium-ion batteries. *Advances in Applied Energy*, **2021**, 4: 100065.

[3] Lu Y, Zhao C Z, Yuan H, et al. Dry electrode technology, the rising star in solid-state battery industrialization. *Matter*, **2022**, 5(3): 876-898.

[4] Marqusee J, Becker W, Ericson S. Resilience and economics of microgrids with PV, battery storage, and networked diesel generators. *Advances in Applied Energy*, **2021**, 3: 100049.

[5] Wang Y, Tian J, Sun Z, et al. A comprehensive review of battery modeling and state estimation approaches for advanced battery management systems. *Renewable and Sustainable Energy Reviews*, **2020**, 131: 110015.

[6] Liu L, Yan Z, Xu B, et al. A Highly Scalable Integrated Voltage Equalizer Based on Parallel-Transformers for High-Voltage Energy Storage Systems. *IEEE Transactions on Industrial Electronics*, **2023**. doi: 10.1109/TIE.2023.3241382.

[7] Lu Y, Zhao C Z, Huang J Q, et al. The timescale identification decoupling complicated kinetic processes in lithium batteries. *Joule*, **2022**, 6(6): 1172-1198.

[8] Hu Y, Wang Y Y. Two time-scaled battery model identification with application to battery state estimation. *IEEE Transactions on Control Systems Technology*, **2014**, 23(3): 1180-1188.

[9] Dai H, Xu T, Zhu L, et al. Adaptive model parameter identification for large capacity Li-ion batteries on separated time scales. *Applied Energy*, **2016**, 184: 119-131.

[10] Osaka T, Mukoyama D, Nara H. Development of diagnostic process for commercially available batteries, especially lithium ion battery, by electrochemical impedance spectroscopy. *Journal of The Electrochemical Society*, **2015**, 162(14): A2529.

[11] Yang B, Wang J, Cao P, et al. Classification, summarization and perspectives on state-of-charge estimation of lithium-ion batteries used in electric vehicles: A critical comprehensive survey. *Journal of Energy Storage*, **2021**, 39: 102572.

[12] Wang Y, Chen Z. A framework for state-of-charge and remaining discharge time prediction using unscented particle filter. *Applied Energy*, **2020**, 260: 114324.

[13] Shi H, Wang L, Wang S, et al. A novel lumped thermal characteristic modeling strategy for the online adaptive temperature and parameter co-estimation of vehicle lithium-ion batteries. *Journal of Energy Storage*, **2022**, 50: 104309.

[14] Che Y, Hu X, Lin X, et al. Health prognostics for lithium-ion batteries: mechanisms, methods, and prospects. *Energy & Environmental Science*, **2023**, 16: 338-371

[15] Wu L, Liu K, Pang H. Evaluation and observability analysis of an improved reduced-order electrochemical model for lithium-ion battery. *Electrochimica Acta*, **2021**, 368: 137604.

[16] Xu L, Lin X, Xie Y, et al. Enabling high-fidelity electrochemical P2D modeling of lithium-ion batteries via fast and non-destructive parameter identification. *Energy Storage Materials*, **2022**, 45: 952-968.

[17] Shi H, Wang S, Wang L, et al. On-line adaptive asynchronous parameter identification of lumped electrical characteristic model for vehicle lithium-ion battery considering multi-time scale effects. *Journal of Power Sources*, **2022**, 517: 230725.

[18] Xiong R, Tian J, Shen W, et al. Semi-supervised estimation of capacity degradation for lithium ion batteries with electrochemical impedance spectroscopy. *Journal of Energy Chemistry*, **2023**, 76: 404-413.

[19] Alavi S M M, Birkl C R, Howey D A. Time-domain fitting of battery electrochemical impedance models. *Journal of Power Sources*, **2015**, 288: 345-352.

[20] Duan Y, Tian J, Lu J, et al. Deep neural network battery impedance spectra prediction by only using constant-current curve. *Energy Storage Materials*, **2021**, 41: 24-31.

[21] Samadani E, Farhad S, Scott W, et al. Empirical modeling of lithium-ion batteries based on electrochemical impedance spectroscopy tests. *Electrochimica Acta*, **2015**, 160: 169-177.

[22] Zhu C, Shang Y, Lu F, et al. Core temperature estimation for self-heating automotive lithium-ion batteries in cold climates. *IEEE Transactions on Industrial Informatics*, **2019**, 16(5): 3366-3375.

[23] Raijmakers L H J, Danilov D L, Eichel R A, et al. A review on various temperature-indication methods for Li-ion batteries. *Applied Energy*, **2019**, 240: 918-945.

[24] Pang H, Wu L, Liu J, et al. Physics-informed neural network approach for heat generation rate estimation of lithium-ion battery under various driving conditions. *Journal of Energy Chemistry*, **2023**, 78: 1-12.

[25] Che Y, Zheng Y, Wu Y, et al. Data efficient health prognostic for batteries based on sequential information-driven probabilistic neural network. *Applied Energy*, **2022**, 323: 119663.

[26] Che Y, Deng Z, Lin X, et al. Predictive battery health management with transfer learning and online model correction. *IEEE Transactions on Vehicular Technology*, **2021**, 70(2): 1269-1277.

[27] Che Y, Deng Z, Li P, et al. State of health prognostics for series battery packs: A universal deep learning method. *Energy*, **2022**, 238: 121857.

[28] Che Y, Stroe D I, Hu X, et al. Semi-supervised self-learning-based lifetime prediction for batteries. *IEEE Transactions on Industrial Informatics*, **2022**, 19: 6471-6481.

[29] Hu X, Che Y, Lin X, et al. Battery health prediction using fusion-based feature selection and machine learning. *IEEE Transactions on Transportation Electrification*, **2020**, 7(2): 382-398.

[30] Severson K A, Attia P M, Jin N, et al. Data-driven prediction of battery cycle life before capacity degradation. *Nature Energy*, **2019**, 4(5): 383-391.

[31] Tian J, Xiong R, Shen W, et al. Flexible battery state of health and state of charge estimation using partial charging data and deep learning. *Energy Storage Materials*, **2022**, 51: 372-381.

[32] Tian J, Xiong R, Lu J, et al. Battery state-of-charge estimation amid dynamic usage with physics-informed deep learning. *Energy Storage Materials*, **2022**, 50: 718-729.

[33] Wang N, Zhao G, Kang Y, et al. Core Temperature Estimation Method for Lithium-ion Battery Based on Long Short-term Memory Model with Transfer Learning. *IEEE Journal of Emerging and Selected Topics in Power Electronics*, **2023**, 11: 201-213.

[34] Wang Y, Xu R, Zhou C, et al. Digital twin and cloud-side-end collaboration for intelligent battery management system. *Journal of Manufacturing Systems*, **2022**, 62: 124-134.

[35] Wang S, Takyi-Aninakwa P, Jin S, et al. An improved feedforward-long short-term memory modeling method for the whole-life-cycle state of charge prediction of lithium-ion batteries considering current-voltage-temperature variation. *Energy*, **2022**, 254: 124224.

[36] Takyi-Aninakwa P, Wang S, Zhang H, et al. An optimized long short-term memory-weighted fading extended Kalman filtering model with wide temperature adaptation for the state of charge estimation of lithium-ion batteries. *Applied Energy*, **2022**, 326: 120043.

[37] Xie Y, Wang S, Zhang G, et al. Optimized multi-hidden layer long short-term memory modeling and suboptimal fading extended Kalman filtering strategies for the synthetic state of charge estimation of lithium-ion batteries. *Applied Energy*, **2023**, 336: 120866.

[38] Li H, Saini A, Liu C, et al. Electrochemical and thermal characteristics of prismatic lithium-ion battery based on a three-dimensional electrochemical-thermal coupled model. *Journal of Energy Storage*, **2021**, 42: 102976.

[39] Lacressonnière F, Varais A, Roboam X, et al. Scale electro-thermal model of a lithium-ion battery for time-accelerated experiments in a hardware in the loop process. *Journal of Energy Storage*, **2021**, 39: 102576.

[40] Xu M, Zhang Z, Wang X, et al. A pseudo three-dimensional electrochemical–thermal model of a prismatic LiFePO4 battery during discharge process. *Energy*, **2015**, 80: 303-317.

[41] Ding Q, Wang Y, Chen Z. Parameter identification of reduced-order electrochemical model simplified by spectral methods and state estimation based on square-root cubature Kalman filter. *Journal of Energy Storage*, **2022**, 46: 103828.

[42] Wang Y, Zhou C, Zhao G, et al. A framework for battery internal temperature and state-of-charge estimation based on fractional-order thermoelectric model. *Transactions of the Institute of Measurement and Control*, **2022**: 01423312211067293. DOI: 10.1177/01423312211067293

[43] Wang Y, Zhou C, Chen Z. Optimization of battery charging strategy based on nonlinear model predictive control. *Energy*, **2022**, 241: 122877.

[44] Shi H, Wang S, Fernandez C, et al. Improved multi-time scale lumped thermoelectric coupling modeling and parameter dispersion evaluation of lithium-ion batteries. *Applied Energy*, **2022**, 324: 119789.

[45] Pang H, Guo L, Wu L, et al. A novel extended Kalman filter-based battery internal and surface temperature estimation based on an improved electro-thermal model. *Journal of Energy Storage*, **2021**, 41: 102854.

[46] Shi H, Wang S, Liang J, et al. Multi-time scale identification of key kinetic processes for lithium-ion batteries considering variable characteristic frequency. *Journal of Energy Chemistry*, **2023**, 82: 521-536.

[47] Tian J, Xu R, Wang Y, et al. Capacity attenuation mechanism modeling and health assessment of lithium-ion batteries. *Energy*, **2021**, 221: 119682.

[48] Jiang C, Wang S, Wu B, et al. A state-of-charge estimation method of the power lithium-ion battery in complex conditions based on adaptive square root extended Kalman filter. *Energy*, **2021**, 219: 119603.

[49] Jiang B, Dai H, Wei X, et al. Joint estimation of lithium-ion battery state of charge and capacity within an adaptive variable multi-timescale framework considering current measurement offset. *Applied Energy*, **2019**, 253: 113619.

[50] Peng J, Shi H, Wang S, et al. A novel equivalent modeling method combined with the splice- electrochemical polarization model and prior generalized inverse least- square parameter identification for UAV lithium- ion batteries. *Energy Science & Engineering*, **2022**, 10(10): 3727-3740.

[51] Wang Y, Zhang X, Chen Z. Low temperature preheating techniques for Lithium-ion batteries: Recent advances and future challenges. *Applied Energy*, **2022**, 313: 118832.

[52] Tian J, Liu X, Chen C, et al. Feature Fusion-Based Inconsistency Evaluation for Battery Pack: Improved Gaussian Mixture Model. *IEEE Transactions on Intelligent Transportation Systems*, **2022**, 24(1): 446-458.

[53] Liu K, Zou C, Li K, et al. Charging pattern optimization for lithium-ion batteries with an electrothermal-aging model. *IEEE transactions on industrial informatics*, **2018**, 14(12): 5463-5474.

[54] Tian J, Wang Y, Chen Z. An improved single particle model for lithium-ion batteries based on main stress factor compensation. *Journal of Cleaner Production*, **2021**, 278: 123456.

[55] Peng S, Sun Y, Yu Q, et al. State of health estimation of lithium-ion batteries based on multi-health features extraction and improved long short-term memory neural network. *Energy*, **2023**, 282: 128956.

[56] Feng X, Ouyang M, Liu X, et al. Thermal runaway mechanism of lithium ion battery for electric vehicles: A review. *Energy Storage Materials*, **2018**, 10: 246-267.